

Topography of the Moon from the Clementine lidar

David E. Smith,¹ Maria T. Zuber,^{2,3} Gregory A. Neumann,⁴
and Frank G. Lemoine⁵

Abstract. Range measurements from the lidar instrument carried aboard the Clementine spacecraft have been used to produce an accurate global topographic model of the Moon. This paper discusses the function of the lidar; the acquisition, processing, and filtering of observations to produce a global topographic model; and the determination of parameters that define the fundamental shape of the Moon. Our topographic model; a 72nd degree and order spherical harmonic expansion of lunar radii, is designated Goddard Lunar Topography Model 2 (GLTM 2). This topographic field has an absolute vertical accuracy of approximately 100 m and a spatial resolution of 2.5°. The field shows that the Moon can be described as a sphere with maximum positive and negative deviations of ~8 km, both occurring on the farside, in the areas of the Korolev and South Pole-Aitken (S.P.-Aitken) basins. The amplitude spectrum of the topography shows more power at longer wavelengths as compared to previous models, owing to more complete sampling of the surface, particularly the farside. A comparison of elevations derived from the Clementine lidar to control point elevations from the Apollo laser altimeters indicates that measured relative topographic heights generally agree to within ~200 m over the maria. While the major axis of the lunar gravity field is aligned in the Earth-Moon direction, the major axis of topography is displaced from this line by approximately 10° to the east and intersects the farside 24° north of the equator. The magnitude of impact basin topography is greater than the lunar flattening (~2 km) and equatorial ellipticity (~800 m), which imposes a significant challenge to interpreting the lunar figure. The floors of mare basins are shown to lie close to an equipotential surface, while the floors of unflooded large basins, except for S.P.-Aitken, lie above this equipotential. The radii of basin floors are thus consistent with a hydrostatic mechanism for the absence of significant farside maria except for S.P.-Aitken, whose depth and lack of mare require significant internal compositional and/or thermal heterogeneity. A macroscale surface roughness map shows that roughness at length scales of 10¹-10² km correlates with elevation and surface age.

Introduction

Topography is one of the principal measurements required to quantitatively describe a planetary body. In addition, when combined with gravity, topography allows the distribution of subsurface density anomalies to be mapped, albeit nonuniquely, yielding information on not only the shape, but also the internal structure of a planet. Such information is fundamental to understanding planetary thermal history. The limited coverage and vertical accuracy of previous topographic measurements have limited the characterization of lunar shape

and structure, and thus interpretation of the implications for the thermal evolution of the Moon. Near-global topographic measurements obtained by the Clementine lidar should enable progress in all of these areas.

The Clementine Mission, sponsored by the Ballistic Missile Defense Organization with science activities supported by NASA, mapped the Moon from February 19 through May 3, 1994 [Nozette *et al.*, 1994]. The spacecraft payload included a light detection and ranging (lidar) instrument that was built by Lawrence Livermore National Laboratory [Nozette *et al.*, 1994]. This instrument was developed for military ranging applications and was not designed to track surface topography. However, by careful programming of instrument parameters, it was possible to cause the ranging device to function as an altimeter and to collect near globally distributed profiles of elevation around the Moon [Zuber *et al.*, 1994]. In this paper, we discuss the Clementine lidar investigation, including the function and performance of the sensor, the collection, processing, and filtering of data, and the development of global models for the geodetically referenced long wavelength shape and higher spatial resolution topography of the Moon. We compare our results to previous analyses of lunar topography and discuss the implications of the improved spatial coverage of the Clementine data as compared to previous data sets.

¹Laboratory for Terrestrial Physics, NASA Goddard Space Flight Center, Greenbelt, Maryland.

²Department of Earth, Atmospheric and Planetary Sciences, Massachusetts Institute of Technology, Cambridge.

³Also at Laboratory for Terrestrial Physics, NASA Goddard Space Flight Center, Greenbelt, Maryland.

⁴Department of Earth and Planetary Sciences, Johns Hopkins University, Baltimore, Maryland.

⁵Space Geodesy Branch, NASA Goddard Space Flight Center, Greenbelt, Maryland.

Copyright 1997 by the American Geophysical Union.

Paper number 96JE02940.
0148-0227/97/96JE-02940\$09.00

Previous Observations

Lunar Topography

Various measurements of lunar elevation have been derived from Earth-based and orbital observations. Earth-based measurements of lunar topography have naturally been limited to the nearside, and include limb profiles [Watts, 1963; Runcorn and Gray, 1967; Runcorn and Shrubbsall, 1968, 1970; Runcorn and Hofmann, 1972], ground-based photogrammetry [Baldwin, 1949, 1963; Hopmann, 1967; Arthur and Bates, 1968; Mills and Sudbury, 1968] and radar interferometry [Zisk, 1971, 1972]. These studies yielded information of limited spatial distribution and positional knowledge of order 500 m.

Orbital data include landmark tracking by the Apollo command and service modules [Wollenhaupt et al., 1972], limb profiles from the Zond-6 orbiter [Rodionov et al., 1971], photogrammetry from the Lunar orbiters [Jones, 1973], and profiling by the Apollo long wavelength radar sounder [Phillips et al., 1973a,b; Brown et al., 1974]. With the exception of the radar sounding data, these observations were not selenodetically referenced to the Moon's center of mass. All of the observations were characterized by absolute errors of the order of 500 m.

More accurate lunar shape information was derived from orbital laser ranging. The Apollo 15, 16, and 17 missions carried laser altimeters which provided measurements of the height of the command modules above the lunar surface [Kaula et al., 1972, 1973, 1974]. The principal objective of these instruments was to provide range measurements to scale images from the Apollo metric cameras [Kaula et al., 1972]. However, accurate orbital range measurements were recognized to be valuable in their own right, and so the altimeters were commanded to range even when the images were not being taken [Kaula et al., 1972]. These measurements provided the first information on the shape of the Moon in a center of mass reference frame.

The Apollo altimeters contained then state-of-the-art ruby flashlamp lasers, whose lifetimes were usually limited by the flashlamp, the function of which was to optically excite the ruby, causing it to lase. However, the very short lifetimes of the Apollo laser altimeters may more logically be explained by failure of mechanically spinning mirrors that controlled the pulsing of the laser. The Apollo altimeters were characterized by a beamwidth of 300 μ rad, illuminating an area of the surface of approximately 300 m in diameter. The vertical accuracy of the instruments, which was controlled by the system oscillator, was ± 2 m. The laser firing interval was varied from 16 to 32 s, resulting in an along-track sampling of the range of the spacecraft to the lunar surface of 30 to 43 km [Kaula et al., 1972; Sjogren and Wollenhaupt, 1973]. The Apollo 15 laser altimeter gathered data for only 2 1/2 revolutions [Roberson and Kaula, 1972; Kaula et al., 1973], while the Apollo 16 [Wollenhaupt and Sjogren, 1972; Kaula et al., 1973] and 17 [Kaula et al., 1974; Wollenhaupt et al., 1974] altimeters obtained data for 7 1/2 and 12 revolutions, respectively. A total of 7080 range measurements was obtained from the three missions, of which 5631 were used in an earlier study of global lunar topography [Bills and Ferrari, 1977] and 5141 are used in a comparison of Apollo and Clementine topography in the present study. The absolute radial accuracy of the Apollo altimetry was approximately 400 m [Kaula et al., 1974], with the greatest uncertainty due to

spacecraft orbit errors largely arising from then current knowledge of the lunar gravity field. The greatest limitation of the Apollo altimeter data is its coverage, which is restricted to $\pm 26^\circ$ of the equator.

Apollo laser altimetry data were used to determine the lunar mean radius of 1737.7 km as well as the offset of the center of figure from the center of mass of -2.55 km in the direction of 25° E [Kaula et al., 1974]. Previous to Clementine, the best spherical harmonic representation of lunar topography was developed by Bills and Ferrari [1977], and consisted of a 12th degree and order model that incorporated the Apollo laser altimeter data, as well as orbital photogrammetry measurements, landmark measurements, and Earth-based photogrammetry and limb profile measurements. The estimated error for these data ranged from 300 to 900 m; however, vast regions of the lunar farside lacked any topography measurements.

Lunar Geodetic Positioning

The locations of the lunar retroreflectors deployed by the Apollo missions and Soviet landers are known to the centimeter level [Dickey et al., 1994]. However, it is not clear how these points can be tied into the present lunar control network [Davies et al., 1987]. Points in the vicinity of the Apollo landers have positional errors of less than 150 m. In the region covered by the Apollo mapping cameras, positional errors increase to approximately 300 m. In regions where telescopic coverage alone is available, positional errors are generally 2 km or less, while in some regions of the farside, errors increase to several kilometers. The degree to which Clementine will ultimately be able to improve geodetic knowledge of the lunar nearside is controlled mainly by the accuracy of spacecraft orbits and the adequacy of the attitude knowledge provided by the spacecraft attitude sensors, both of which are discussed in this analysis.

Measuring Lunar Topography

The Clementine Lidar

The Clementine lidar is shown in Figure 1, and its specifications are given in Table 1. This laser transmitter, which was built by McDonnell-Douglas Space Systems Division in St. Louis, contained a neodymium-doped yttrium-aluminum-garnet (Nd:YAG) source that produced lasing at a wavelength of 1.064 μ m. The laser had a pulsewidth of <10 ns, a pulse energy of 171 mJ, and a beam divergence of <500 μ rad, which resulted in a surface spot size near the minimum spacecraft orbital altitude (periselene \sim 400 km) of \sim 200 m. The lidar receiver included an aluminum cassegrain telescope that was shared with the Clementine high resolution (HIRES) camera. Incident photons collected by the telescope were focused onto a silicon avalanche photodiode (SiAPD) focal plane array.

During its 2 months at the Moon, the Clementine spacecraft orbited within ranging distance for approximately one-half hour per 5-hour orbit, and the lidar collected data during most of this time. During the first month, with spacecraft periselene at latitude 30° S, topographic profiles were obtained in the latitude range 79° S to 22° N. In the second month of mapping, with spacecraft periselene at latitude 30° N, profiles were obtained in the latitude range 20° S to 81° N. The along-

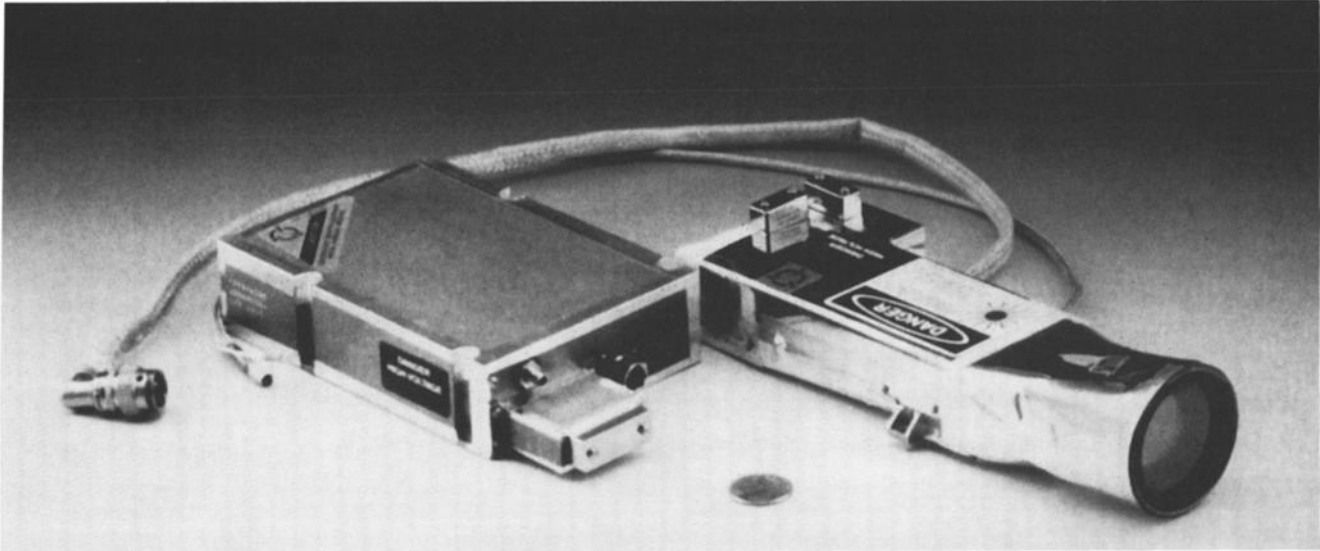


Figure 1. The Clementine ranging lidar, consisting of a 0.131 m diameter Cassegrain telescope (right), a 1.064- μm Nd:YAG laser transmitter (left), and receiver electronics (not shown). The instrument was designed and built at Lawrence Livermore National Laboratory, Livermore, California, except for the laser transmitter, which was built by McDonnell-Douglas Space Systems Division, St. Louis, Missouri.

track shot spacing assuming a 100% laser ranging probability is ~ 20 km, and this resolution was achieved over some smooth mare surfaces. However, as detailed later, in rough highland terrains where the instrument did not maintain "lock" with the surface, the spacing was more typically of the order of 100 km. The across-track resolution was governed by mission duration,

i.e., the spacing of orbital tracks, and is approximately 60 km at the equator and less elsewhere.

Geodetic Conventions

The Clementine spacecraft and instruments utilized two coordinate systems: (1) a spacecraft-fixed XYZ coordinate system along whose axes the spacecraft inertial measurement units (IMU) were aligned to measure the spacecraft attitude and thus the inertial pointing of the science instruments; and (2) a science instrument-fixed xyz coordinate system used to define the mounting of each instrument with respect to the spacecraft-fixed XYZ system, instrument pointing, and the observation geometry within each instrument. The Earth Mean Equator and Vernal Equinox 2000 (i.e., J2000) was used as the standard inertial reference system to describe the Clementine spacecraft trajectory, planetary body ephemerides, star positions, inertial orientations of planetary body-fixed coordinate systems, inertial spacecraft attitude, and inertial instrument pointing. A series of matrix transformations was used to relate the instrument-fixed coordinates to the inertial J2000 coordinates [Duxbury *et al.*, 1994]. All calculations for topography were done in a mass-centered, selenocentric coordinate reference system, with longitude defined as positive eastward with the prime meridian defined as the mean sub-Earth longitude [Davies *et al.*, 1987].

Orbit and Range Determination

In order to determine a global topographic data set from the Clementine lidar system it was necessary to compute precise spacecraft orbits, which were subtracted from the range profiles to yield relative surface elevations. We computed these orbits [Lemoine *et al.*, 1995] with the Goddard Space Flight Center's GEODYN/SOLVE orbital analysis programs [Putney, 1977; McCarthy *et al.*, 1994], which are batch processing programs that numerically integrate the spacecraft

Table 1. Clementine Ranging Lidar Instrument Parameters

Parameter	Value	Unit
Laser		
Type	Nd:YAG	
Wavelength	1.064	mm
Energy	171	mJ
Pulse width	10(?)	ns
Beam divergence	500	mrاد
Nominal pulse repetition rate	0.6	Hz
Detector		
Type	SiAPD	
Field of view	0.057	degrees
Bandpass filter	0.4 to 1.1	mrاد
Telescope		
Type	Cassegrain	
Diameter	0.131	m
Focal length	0.125	m
Receiver electronics		
Clock counter	14	bits
Frequency response	15.0001	MHz
Return range bin	39.972	m
Maximum range	640	km
Gain	100x	
Other		
Spot size at periselene	~ 200	m
Assumed lunar albedo	0.15 to 0.5	
Minimum along-track shot spacing	20	km
Instrument		
Mass	2.370	kg
Power	6.8 at 1 Hz	W

Cartesian state and force model partial derivatives by utilizing a high-order predictor-corrector model. The force model for this study included spherical harmonic representations of the lunar and terrestrial gravity fields (a low-degree and -order model, only, for the latter), as well as point mass representations for the Sun and other planets. Estimates for solar radiation pressure, tidal parameters, planetary rotation, measurement and timing biases, and tracking station coordinates were obtained along with the orbits. Spacecraft jet firings to relieve attitude disturbance torques (aka momentum dumps) were accounted for by explicitly estimating them in the orbit determination process or by breaking orbital arcs at the times of the maneuvers.

To determine the range of the spacecraft to the lunar surface, we interpolated the spacecraft orbital trajectory to the time of the laser measurement, and corrected for the one-way light time to the surface. We then transformed the measured range from the spacecraft to the surface to a lunar radius in a center of mass reference frame. Our orbits were characterized by a repeatability in radial position of about 10 m and have a radial accuracy with respect to the lunar center of mass of approximately 70 m [Lemoine *et al.*, 1995].

Sources of Radial Error

In Table 2 we list estimates of the sources of radial error for the Clementine lidar system. Principal error sources include orbit, which we estimate at 3 times the radial position repeatability of 10 m, and the system error of the instrument, which comes from the least significant bit in the system oscillator (40 m). Errors in knowledge of the lunar geoid, which affect referencing of the topographic model, are estimated to be of the order of 10 m. The pointing errors from the spacecraft around the Moon were generally at the milliradian level [Regeon *et al.*, 1994], which after correction using the spacecraft quaternions translated to, at most, meter-scale errors. (However, during several passes, the spacecraft was intentionally pointed off-nadir for imaging of specific targets. The lidar successfully ranged at angles of up to 6° off-nadir, though in general, off-nadir angles of greater than 4° yielded ranges with unacceptably large errors and were discarded.) The roughness of the lunar surface is another significant error source. A roughness corresponding to a

footprint-scale surface slope of 5°, typical of rough highland terrains, gives an error of 17 m. Postprocessing revealed jitter equivalent to approximately one range bin (~40 m) in the data. Range walk, the error in knowledge of the centroid of the return pulse that arises due to pulse spreading, may produce an error of as much as 70 m.

Since the error sources are statistically independent, we may estimate the total error from the root sum square of the contribution, and doing so yields a total radial error of approximately 100 m. A 30% contingency to account for additional unmodeled or mismodeled error sources yields a radial error of 130 m.

The Laser Ranging Process

The lidar measured the slant range of the spacecraft to the lunar surface at spacecraft altitudes of 640 km or less [Nozette *et al.*, 1994]. The range was determined by the number of clock cycles between the laser start pulse and returned signal. The analog/digital (A/D) resolution of the lidar clock was limited by a 14-bit chip, which was used owing to its availability on the accelerated development schedule of the Clementine Project. Owing to the limitations of this chip, it was necessary to bin four returns to each clock count, which produced a single shot range resolution of 39.972 m.

After each laser shot, the lidar electronics triggered continuously on the arrival of photon pulses above a voltage threshold while the range counter incremented. Noise from the SiAPD detector or solar background radiation at the laser wavelength would often trigger the electronics before any photons from the laser shot would arrive. After detecting the reflected pulse, further noise triggers persisted. In order to record only "reasonable" lunar range counts, a range window, defined as a period of time during which a returned laser pulse was expected, was programmed to maximize the probability of valid returns via uploaded commanding. Illustrated in Figure 2, the window setting was determined from orbital predictions, surface albedo (mare versus highland), Sun angle, and instrument gain; the settings were modified several times during each orbital pass by the instrument engineers and science team. The counts associated with the last trigger before the window; the first, second, third, and last trigger within the window; and the first trigger after the window were

Table 2. Sources of Radial Error in GLTM 2

Error Source	Approximate Magnitude, m	Comment
Lidar instrument	40	measured; instrument performance
Orbit repeatability (radial)	30	calculated; 3x formal error
Geoid	10	calculated
Spacecraft pointing	10	estimated; assumes 10x poorer performance than nominally observed
Range jitter	40	observed
Footprint-scale surface roughness	17	calculated; assumes 5° variation over footprint
Range walk	70	estimated; assumes 45° slope
RSS*	97	
Contingency	30	
RSS including contingency	127	

*RSS, root sum square.

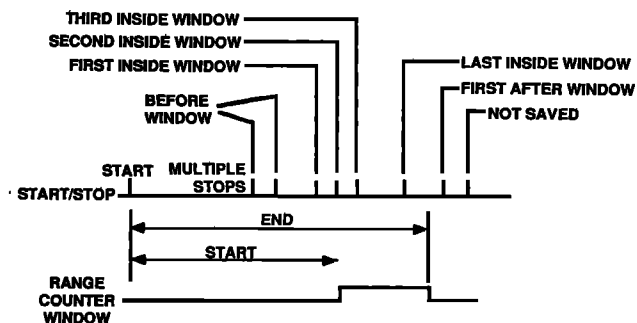


Figure 2. Clementine lidar range counter latches. The receiver electronics was designed such that a single transmitted laser pulse could report up to four measurements of range, corresponding to the first three and last "hits" within the range window. A range was reported when the number of photons incident on the instrument detector exceeded the user-defined detection threshold. "False triggers" were due to noise from the system electronics and solar background radiation at the laser wavelength that was received directly or reflected from the Moon. The range window position and width and the threshold settings were uploaded via ground commanding and were modified several times during each orbital pass.

latched into registers 0-5. If fewer than four triggers occurred within the range window, the last count within the gate was identical to the previous trigger. Initial results suggested that later returns were increasingly likely to be due to noise, but depending on how soon the range window opened, any of the early returns could also be due to noise. The procedure that we implemented to distinguish between multiple triggers for a given transmitted pulse is discussed below.

Laser ranging was performed on orbital passes 8 to 163 in the southern hemisphere and passes 165 to 332 in the north. Figure 3 compares the topographic coverage obtained by Clementine compared to that by the Apollo 15, 16, and 17 laser altimeters. Passes 8 through 19 were calibration passes, and the data were discarded due to poor quality. During the course of the mapping mission the lidar triggered on about 123,000 shots, corresponding to 19% of the transmitted laser pulses. Much of the time, the first trigger in the range window was a true echo, but often, particularly over rough terrain, there were multiple ("false") triggers due to noise that did not correlate with lunar features. The main sources of noise were the clock jitter, roughly normally distributed with ~ 40 m sigma; side-lobe artifacts from the laser transmitter, which are terrain-dependent and not well understood; detector noise, which is dependent on ambient conditions (especially temperature variations on the SiAPD detector), range and threshold settings, and link margin; and solar background radiation at the laser wavelength, imparted directly on to the detector and reflected from the lunar surface. In order to develop a digital topographic model of the Moon, it was necessary to develop a filter that, when applied to the data, returned at most a single valid range value for each bounce point. Since the detailed topography was largely unknown, it was necessary for this filter to be based on a priori knowledge of lunar surface properties. In the following section we describe a stochastic model for topography, its associated parameters, and a procedure that implemented this model as a filter.

Processing Lunar Topography

Stochastic Description of Topography

One-dimensional (1-D) topographic profiles often obey a power law [Bell, 1975] for spectral power P , as a function of wave number $k=1/\lambda$, of the form

$$P(k) = ak^{-b} \quad (1)$$

where constants a and b are the intercept and slope on a log-log plot. Topographic spectra are invariably "red," that is, fall off at high wave numbers, with b ranging from 1 to 3 [Sayles and Thomas, 1978; Huang and Turcotte, 1989]. The same relation applies to two-dimensional (2-D) spectra, as a function of wave number magnitude $|k|$, with b from 2 to 4 [Goff, 1990]. Planets obey a similar expression for spherical harmonic gravity coefficients known as Kaula's rule [Kaula, 1966]. For planetary surfaces the value of b for coefficient variances is asymptotically equal to 3 [Bills and Kobrick, 1985].

A related local scaling property of surfaces described by a function $z(x)$ is that they are statistically self-affine [Mandelbrot, 1982; Goff, 1990; Malinverno, 1991]. This means that for any constant $a > 0$, there is a neighborhood $|u| < \epsilon$ of any given point x where the probability distribution of differences $z(x+au) - z(x)$ is the same as that of $[z(x+u) - z(x)]$ times a scale factor a^H , where H is the Hurst exponent [Hurst, 1951]. Viewing a small piece of terrain at greater horizontal and vertical magnification does not change its essential appearance. The self-affine property implies a fractal dimension $D = 3 - H$, and for most power law surfaces, $D = 4 - b/2$ [Goff, 1990]. Planetary surfaces have

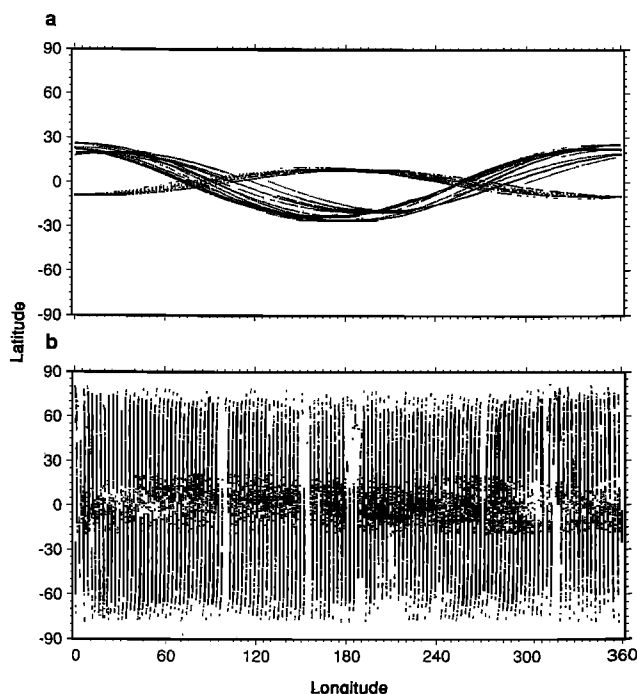


Figure 3. (a) Locations of laser topographic measurements from the Apollo 15, 16, and 17 laser altimeters. (b) Locations of laser topographic measurements from the Clementine Lidar. The points shown are those remaining after filtering to remove spurious noise hits.

been described in terms of a fractional Brownian model, for which H ranges from 0.5 to 0.95 [Mandelbrot, 1975, 1982]. In such models, repeated random displacements generate a self-affine, fractal surface. Thus the mesoscale lunar highland surface, being saturated by uncorrelated impact processes of random size and distribution, is roughly self-affine.

At intermediate scales on the Earth, the spectral amplitudes of long-wavelength topography are attenuated by viscous relaxation and are smaller than predicted by a single power law [Fox and Hayes, 1985; Gilbert and Malinverno, 1988; Goff and Jordan, 1988]. Below some corner wave number k_0 , the reciprocal of wavelength, spectral power flattens, and the topographic variance is bounded by the square of a characteristic height h . Such characteristic height and width scales have been incorporated into a 2-D stochastic model for seafloor topography [Goff and Jordan, 1988, 1989a,b], via a stationary, random function, which is completely specified by its covariance. The covariance, assuming a zero mean, is the second-order moment of a topographic function $z(x)$:

$$c(u) = \langle z(x+u)z(x) \rangle, \quad (2)$$

with the brackets indicating an average over points where the product is defined. Goff and Jordan [1988] parameterize the covariance in the isotropic case, for $r = k_0 |u|$, as

$$c(u) = h^2 G_\nu(r) / G_\nu(0), \quad (3)$$

where $G_\nu(r) = r^\nu K_\nu(r)$ and K_ν is the modified Bessel function of the second kind, of order ν . For $\nu=0.5$ the covariance takes the simple form $c(u) = \exp(-r)$. The covariance model parameter ν , which describes the scaling behavior of topography at shorter length scales, determines the fractal dimension $D = 3 - \nu$ [Goff and Jordan, 1988] and the falloff of the 2-D power spectrum,

$$P(k) = 4\pi\nu h^2 k_0^{-1} [k^2 + 1]^{-(\nu+1)}, \quad (4)$$

from which it is clear that for large wave numbers the spectral power falls off as $|k|^{-2(\nu+1)}$.

Given a covariance function describing the correlation properties of the topography, and given a set of observations $z(x_i)$ with associated standard deviations σ_i , an interpolation scheme [Tarantola and Valette, 1982] allows us to predict the elevation at an arbitrary point x , together with confidence limits. This procedure, also known as kriging [Matherton, 1965], generalizes the steady state Kalman filter [Kalman, 1960].

For zero-mean topographic functions, the estimate \hat{z} is given by

$$\hat{z}(x) = \sum_i \sum_j c(x_i - x) S_{ij}^{-1} z(x_j), \quad (5)$$

where $S_{ij} = c(x_i - x_j) + \delta_{ij} \sigma_i \sigma_j$. The variance of each estimate is given by

$$\sigma^2(x) = c(0) - \sum_i \sum_j c(x_i - x) S_{ij}^{-1} c(x_j - x). \quad (6)$$

The linear system is solved by an incrementally updated Cholesky factorization for symmetric, positive-definite matrices [Press et al., 1986].

The interpolant $\hat{z}(x)$ is a least squares, unbiased estimate of the elevation at any particular point, given the observations and an a priori topographic distribution with zero mean and covariance $c(u)$. In order to apply it as a filter, we evaluate the observations in sequence. An elevation z is accepted if it lies within a confidence interval of $\hat{z}(x)$. It is incorporated into the topographic model, and the next interpolant is calculated, together with its confidence interval. Such a filter tracks the lunar surface while rejecting most of the noise. Initial experience with multiring basins such as Orientale found that the filter would track up to the edge of the crater rim but would "lose lock" as the topography dropped off abruptly and exceeded the confidence limits. A few of the noise returns would be accepted and some of the valid hits rejected, until the confidence limits increased and the filter found the crater floor. Filtering in the reverse direction from the spacecraft pass would track the floor and then miss the abrupt rise. Thus forward and backward filtering is required.

The modified filtering algorithm proceeds as follows: each orbital pass for which range data exist is filtered in sequence. Elevations with respect to the dynamical ellipsoid are tested with respect to the stochastic model to see whether they lie within the confidence limits. If so, the elevation is flagged as acceptable, and the model is updated. Thus, at this stage, more than one range count may be included for each shot. Next, the pass is filtered in reverse order, and acceptable ranges are flagged. The union of the forward and backward pass provides a list of ranges for this pass that make the "first cut."

The first cut incorporates a considerable amount of noise and often deviates substantially from the "true" surface returns. The confidence limits of the model are based on the number of "valid" observations in the vicinity of the interpolant and are thus narrower than in the forward or backward passes. The next cut is formed by augmenting the confidence limits with an added initial tolerance of 2 km. To eliminate noise while maintaining "lock" on the planetary surface, the model is iteratively refined by successive reduction of the added tolerance by one half. The resulting models reject a greater proportion of noise returns. When no further returns are rejected, the results from the current orbital pass are added to the filtered data set, and we proceed to the next pass.

The filtered data set grows with each succeeding pass, until nearly all of the southern hemisphere is filtered. The second month's mapping of the northern hemisphere overlaps in the region from 15°S to 15°N latitude, so that the constraints from the first month provide added stability to the filter near the equator. The computational burden of equations (5) and (6) grows as the cube of the number of observations, so it became necessary to limit the model for each orbital pass to passes within 5.6° of longitude. This was sufficient to include at least two of the adjacent orbits east or west of the pass, more in the region of overlap near the equator.

Given prior data, we adopted the values $h = 8$ km and found that a correlation distance of 170 km, about 5.6° of latitude, gave good results. Initial experience with orbital passes over Orientale Basin provided estimates of the standard deviations of first through fourth returns of 2, 5, 8, and 15 km, respectively. These standard deviations are representative of the unfiltered data set as a whole. Without any false returns, electronic jitter and quantization are responsible for an uncorrelated noise whose standard deviation is about 40 m, while radial orbital uncertainty is of the order of 100 m

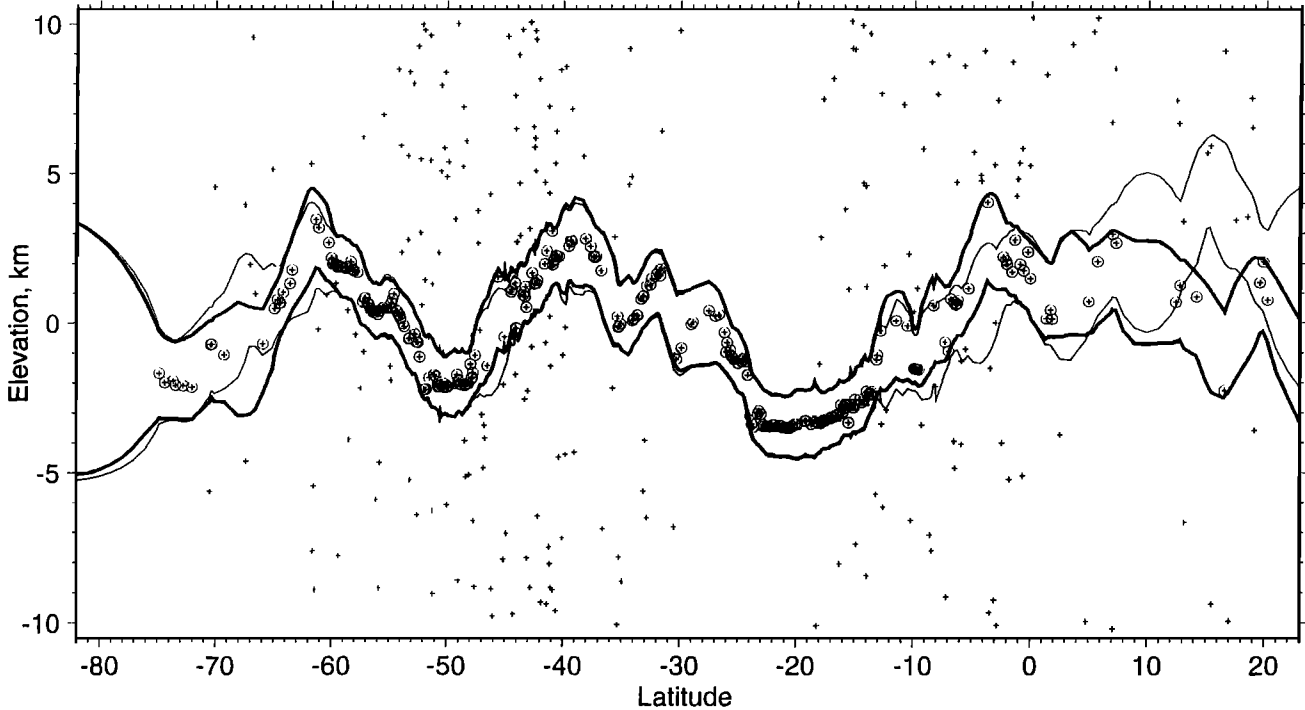
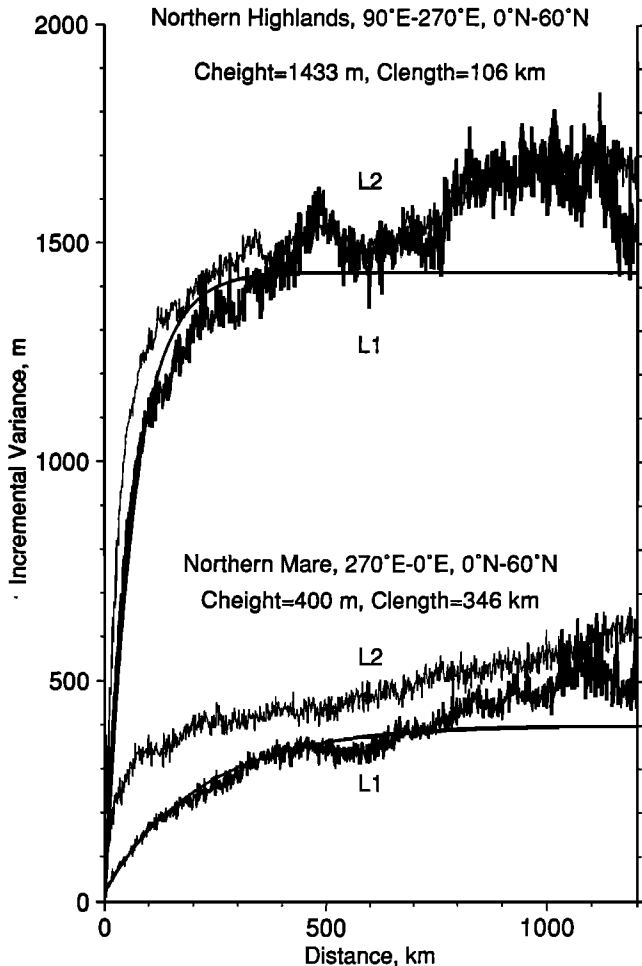


Figure 4. Results of Kalman filter of lidar range measurements for Clementine orbit 71. Range values that were accepted by the filter are noted by circled plus signs. The dark lines represent the range of acceptable elevations determined by the filter. Light lines denote the limits of acceptable ranges before adjacent passes are taken into account.



[Lemoine et al., 1995]. Filtering the data yielded 72,548 valid ranges that were used to generate a global lunar topographic grid and spherical harmonic model. After filtering, a few dozen ranges corresponding to known impact features were manually included, and a small number of suspect ranges were excluded. Figure 4 shows an example of a filtered pass over Mare Orientale and the Mendel-Rydberg Basin.

Assessment of the Stochastic Topographic Model

A convenient way to represent the covariance of surfaces is the incremental variance $\gamma(u) = \frac{1}{2} \langle (\Delta z)^2 \rangle$ [Matherton, 1965; Davis, 1973], the variance of differences $\Delta z = z(x+u) - z(x)$. For stationary, random, zero-mean functions, gamma is related to the covariance by

$$\gamma(u) = c(0) - c(u). \tag{7}$$

The incremental deviation $d(u) = \sqrt{\gamma(u)}$ expresses the average local slope of the surface and asymptotically reaches the characteristic height or roughness. Figure 5 shows lunar

Figure 5. Lunar incremental deviation with offset for northern hemisphere mare and highland regions. The mare regions are extraordinarily smooth, while farside highland regions are much rougher and have a shorter characteristic correlation length. The figure plots both the sum-of-squares (L_2) standard deviation and the more robust L_1 deviation [Neumann and Forsyth, 1995] and parameterized fits. For distances of less than 100 km the deviations increase nearly linearly, especially when robust estimates are used. The deviations justify our application of a self-similar model over a few degrees of scale.

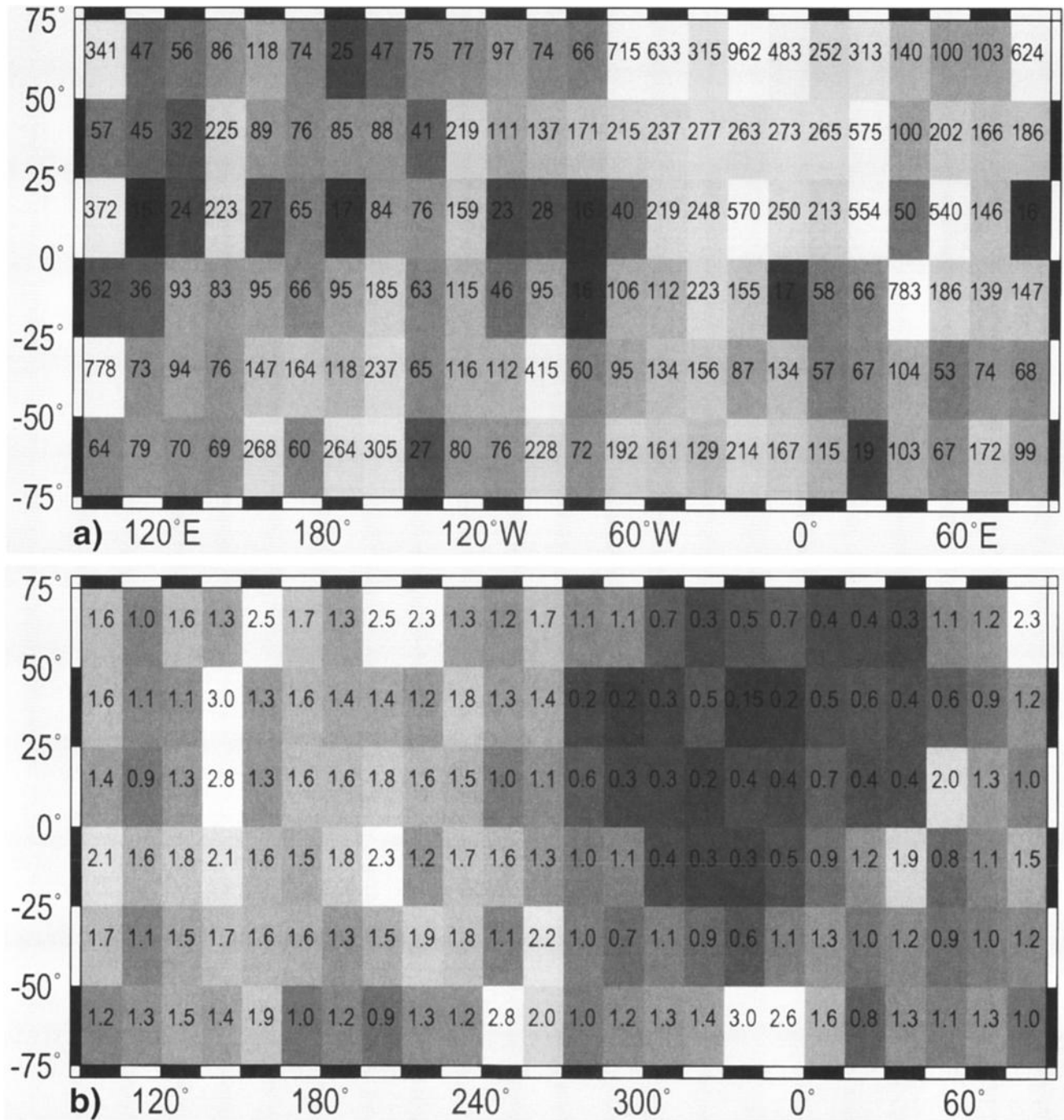


Figure 6. Macroscale surface roughness of the Moon in $30^\circ \times 25^\circ$ squares. (a) Characteristic height (h) in kilometers. (b) Characteristic length ($1/k_0$) in kilometers. Both maps are characterized by 15° by 25° regions from 75° S to 75° N based on a grid of observations based on a resolution of $1/20^\circ$. Roughness was determined by fitting the local along-track and across-track slopes to the covariance model used in the altimetry filtering scheme.

incremental deviation with offset for northern hemisphere mare and highland regions. The mare regions are extraordinarily smooth in topography despite large gravity anomalies [Zuber *et al.*, 1994]. The farside highland regions are much rougher and have a shorter characteristic length.

Populations of differences Δz are generally long-tailed and contain outliers. We show both the sum-of-squares (L_2) standard deviation, and the more robust L_1 deviation [Neumann

and Forsyth, 1995] and parameterized fits. For distances of less than 100 km, especially when robust estimates are used, the deviations increase nearly linearly. While other stochastic models may provide a better fit to the large-scale topography, Figure 5 justifies our use of a self-similar model over a few degrees of scale.

The stochastic parameters that best fit the topography vary markedly over the lunar surface. Figure 6 shows h and k_0 for 15° by 25° regions from 75° S to 75° N based on a grid of

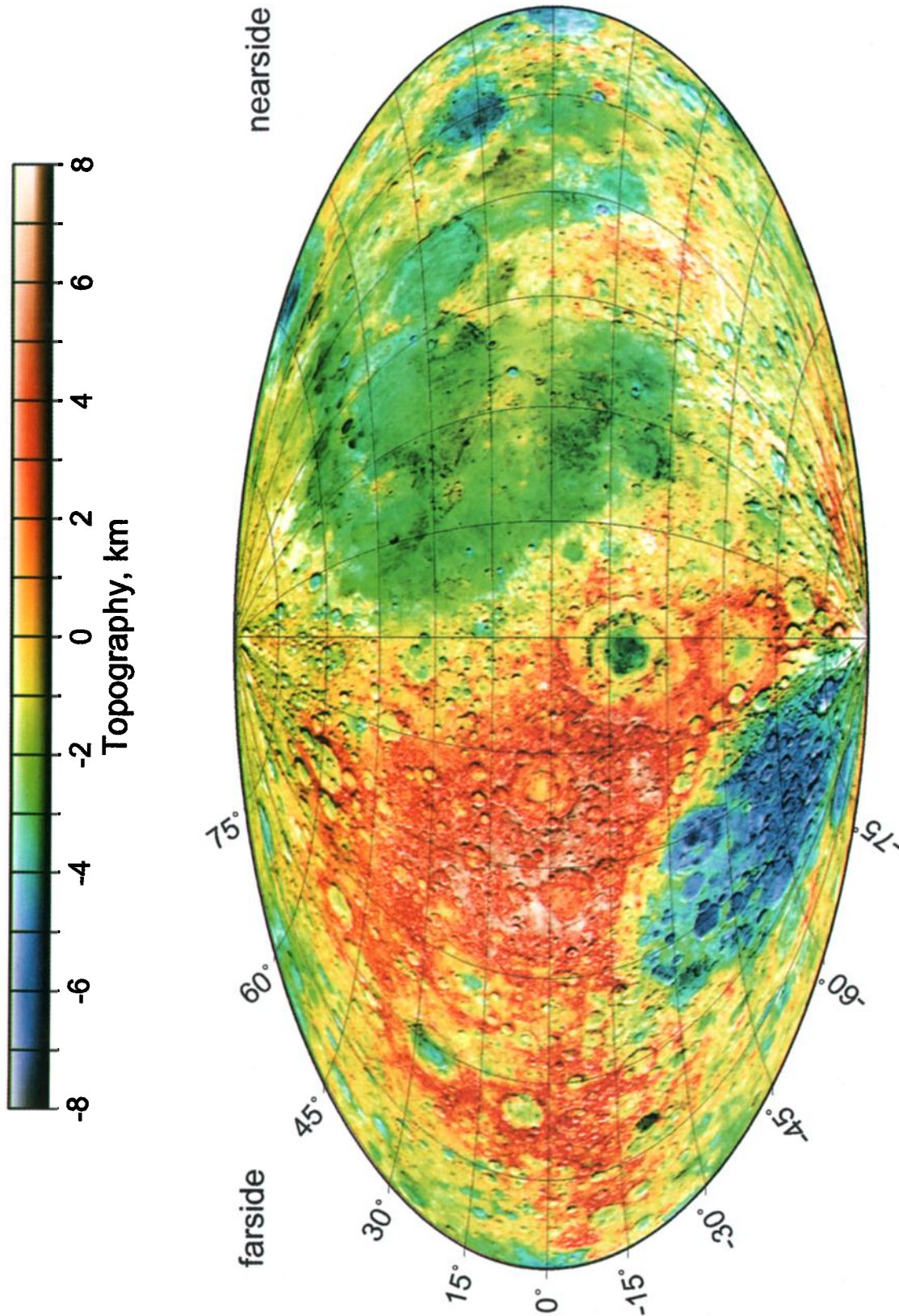


Plate 1. Topography of the Moon from the Clementine ranging lidar. The map is a Hammer equal-area projection centered on 270°E , with nearside on the right and farside on the left. The longitude grid lines are at 30° intervals, and latitude grid lines are at 15° intervals. The coordinate system is selenocentric with an east-positive longitude convention. The dynamic range of topography revealed by Clementine is 16 km. Note that the highest (205°E , 5°N) and lowest (180°E , 56°S) elevations on the Moon occur in adjacent regions on the farside.

Table 3. Spherical Harmonic Normalization Factors

Degree	Order	Factor
0	0	1
1	0	$\sqrt{3}$
1	1	$\sqrt{3}$
2	0	$\sqrt{5}$
2	1	$\sqrt{5/3}$
2	2	$(1/2)\sqrt{5/3}$
3	0	$\sqrt{7}$
3	1	$\sqrt{7/6}$
3	2	$(1/2)\sqrt{7/15}$
3	3	$(1/6)\sqrt{7/10}$
4	0	$\sqrt{9}$
4	1	$\sqrt{9/10}$

Factor(l, m) = $\sqrt{[(l-m)!(2l+1)(2-\delta)/(l+m)!]}$, where $\delta = 1$ for $m = 0$, $\delta = 0$ for $m \neq 0$. From *Kaula* [1966].

observations based on a resolution of $1/20^\circ$. These maps will later be interpreted in terms of macroscale roughness of the lunar surface at length scales of 10^1 - 10^2 km.

Spherical Harmonic Model

The filtered data were assembled into a $0.25^\circ \times 0.25^\circ$ grid, corresponding to the minimum spacing between orbital passes. Figure 3b shows that most major lunar basins were sampled by Clementine altimetry. The lidar did not return much ranging information poleward of $\pm 78^\circ$. Consequently, before performing a spherical harmonic expansion of the data set, it was necessary to interpolate over the polar regions, corresponding to $\sim 2\%$ of the planet's surface area. For this purpose, we used the method of splines with tension [*Smith and Wessel*, 1990] to continue the data smoothly across the poles. We performed a spherical harmonic expansion of the mass-centered radii and the interpolated polar regions to yield a global model of topography H of the form

$$H(\lambda, \phi) = \left[\sum_{l=1}^N \sum_{m=0}^l \bar{P}_{lm}(\sin \phi) (\bar{C}_{lm} \cos m\lambda + \bar{S}_{lm} \sin m\lambda) \right] \quad (8)$$

where ϕ and λ are the selenocentric latitude and longitude of the surface, \bar{P}_{lm} are the normalized associated Legendre functions of degree l and azimuthal order m , \bar{C}_{lm} and \bar{S}_{lm} are the normalized spherical harmonic coefficients with units given in meters, and N is the maximum degree representing the size (or resolution) of the field. Here the C and S coefficients provide information on the distribution of global topography. We have designated our spherical harmonic expansion of topography, performed to degree and order 72, Goddard Lunar Topography Model 2 (GLTM 2). The model, shown in Plate 1, has a full wavelength spatial resolution of ~ 300 km. The spherical harmonic solution is normalized in the manner of *Kaula* [1966]; normalization factors are given in Table 3. Spherical harmonic coefficients for the first 16 degrees and orders are included in Table 4.

Topography of the Moon

Global Attributes

GLTM 2 represents a refinement of our earlier solution GLTM 1 [*Zuber et al.*, 1994], which represented the first

reliable global characterization of surface heights for the Moon. Comparison of the data content and size of the model to the pre-Clementine solution of *Bills and Ferrari* [1977] is presented in Table 5. To first order, the shape of the Moon can be described as a sphere with maximum positive and negative deviations of ~ 8 km, both occurring on the farside (240°E , 10°S ; 160°E , 75°S) in the areas of the Korolev and South Pole-Aitken (S.P.-Aitken) basins, respectively. Departures from sphericity are the result of the processes that shaped the Moon (e.g., impact, volcanism, rotation, tides) early in its history [*Zuber et al.*, 1996]. As detailed in the next section, the largest global-scale features are the center-of-mass/center-of-figure (COM/COF) offset and the polar flattening, both of which are of the order of 2 km, and the equatorial ellipticity, which is slightly less than 1 km. However, there are significant shorter wavelength deviations, due primarily to impact basins, that are much larger.

Figure 7 plots the square root of the sum of the squares of the spherical harmonic C and S coefficients for a given degree l (8), i.e., the power per degree. This amplitude spectrum of the topographic model has more power at longer wavelengths than previous models owing mostly to more complete sampling of the surface, particularly the lunar farside. The figure demonstrates that the power of topography follows a simple general relationship of 2 km/spherical harmonic degree.

Another fundamental characteristic of the lunar shape is that the topographic signatures of the nearside and farside are very different. As shown in Figure 8, the nearside has a gentle topography with an rms deviation of only about 1.4 km with respect to the best fit sphere compared to the farside, for which the deviation is twice as large. The shapes of the histograms of the deviations from the sphere show a peaked distribution slightly skewed toward lower values for the nearside, while the farside is broader but clearly shows S.P.-Aitken as an anomaly compared to the rest of the hemisphere. The sharpness of the nearside histogram is a result of the maria, which define an equipotential surface (cf. Figure 15).

We have performed a comparison of elevations derived from the Clementine lidar to control point elevations from the Apollo laser altimeters [*Davies et al.*, 1987]. A summary of the Clementine and Apollo data sets is presented in Table 6. Figure 9 indicates that where Apollo and Clementine coverage overlaps, measured relative topographic heights generally agree to within ~ 200 m, with most of the difference due to our more accurate orbit corrections [*Lemoine et al.*, 1995] and to variations in large-scale surface roughness (Figure 6). In contrast, Clementine topography often differs from landmark elevations on the lunar limb [*Head et al.*, 1981] by as much as several kilometers.

Differences in lunar shape parameters derived from a comparison of Clementine and Apollo are mostly due to Apollo's coverage being limited to north and south latitudes 26° and below. The greatest differences are on the farside over a broad latitude band, much of which was not properly sampled by the Apollo laser instruments.

Fundamental Parameters of the Shape

The Clementine altimetry data have made possible improved estimates of the fundamental parameters of the Moon's shape, which are principally derived from the long-wavelength field. To isolate the relevant parameters, we performed several least squares spherical harmonic expansions of the Clementine gridded altimetric radii sampled at a

Table 4. Normalized Coefficients of the 16 x 16 Lunar Shape Model

Degree	Order	Coefficient		Degree	Order	Coefficient		Degree	Order	Coefficient	
		\bar{C}	\bar{V}			\bar{C}	\bar{V}			\bar{C}	\bar{V}
0	0	1,737,094		9	6	29	-27	13	11	-1	9
1	0	162		9	7	-38	-39	13	12	-22	20
1	1	-1007	-424	9	8	76	-124	13	13	-6	-73
2	0	-733		9	9	34	26	14	0	46	
2	1	-777	1	10	0	-49		14	1	-42	4
2	2	72	395	10	1	21	13	14	2	15	16
3	0	99		10	2	-21	13	14	3	60	20
3	1	559	66	10	3	6	-57	14	4	24	9
3	2	456	158	10	4	-27	66	14	5	11	33
3	3	433	-10	10	5	-12	60	14	6	25	-6
4	0	202		10	6	-17	45	14	7	26	36
4	1	-199	-54	10	7	37	55	14	8	5	61
4	2	-311	-88	10	8	40	21	14	9	-26	-26
4	3	-213	-274	10	9	69	16	14	10	-4	4
4	4	-220	110	10	10	86	13	14	11	-10	15
5	0	-84		11	0	23		14	12	-15	-37
5	1	22	-22	11	1	-6	-2	14	13	-28	-30
5	2	160	140	11	2	1	42	14	14	6	-34
5	3	5	200	11	3	-14	106	15	0	0	
5	4	48	11	11	4	0	-22	15	1	-28	-23
5	5	125	-73	11	5	46	16	15	2	-11	20
6	0	-4		11	6	-16	-18	15	3	-36	-28
6	1	100	-134	11	7	38	14	15	4	16	-12
6	2	-13	-98	11	8	0	12	15	5	-29	19
6	3	-39	-67	11	9	26	9	15	6	53	-28
6	4	-87	-127	11	10	-7	8	15	7	31	30
6	5	-51	-154	11	11	-9	57	15	8	52	-1
6	6	29	112	12	0	-33		15	9	-9	20
7	0	107		12	1	-10	9	15	10	-4	18
7	1	161	30	12	2	24	0	15	11	40	-29
7	2	80	14	12	3	-25	-55	15	12	-28	-18
7	3	-22	108	12	4	-37	3	15	13	58	40
7	4	-19	49	12	5	-1	-36	15	14	-25	74
7	5	-25	103	12	6	0	4	15	15	49	-7
7	6	-107	42	12	7	11	60	16	0	6	
7	7	1	-29	12	8	-9	-8	16	1	-23	-11
8	0	77		12	9	-15	79	16	2	33	6
8	1	-121	35	12	10	-46	-17	16	3	-7	-26
8	2	-23	54	12	11	85	71	16	4	31	36
8	3	4	55	12	12	-94	81	16	5	16	35
8	4	147	-38	13	0	-15		16	6	9	31
8	5	44	58	13	1	41	-43	16	7	6	-6
8	6	1	-35	13	2	-76	-49	16	8	-33	-23
8	7	42	-1	13	3	6	-33	16	9	-17	-75
8	8	-25	80	13	4	-27	-5	16	10	17	2
9	0	-7		13	5	10	-69	16	11	-17	-9
9	1	79	18	13	6	-6	-4	16	12	-16	29
9	2	2	-29	13	7	8	-66	16	13	-10	0
9	3	4	-1	13	8	-20	-7	16	14	17	-44
9	4	-93	-57	13	9	-27	-46	16	15	30	13
9	5	-56	-113	13	10	19	-9	16	16	-16	-28

Values are in units of meters.

resolution of $2^\circ \times 2^\circ$ and examined the stability of solutions over a range of low degrees and orders.

Mean, equatorial, and polar radii. Figure 10 shows solutions for mean, equatorial, and polar radii. Based on the average of nine low-degree solutions, we define the mean radius of the Moon to be $1,737,103 \pm 15$ m. Table 7 lists values of the mean, equatorial, and polar radii for a range of low-degree spherical harmonic models. The small variation in the solutions for different degrees and orders suggests to us that these parameters are reasonably well determined from the Clementine data. However, the variations in the values across the different solutions have probably not captured any systematic error common to all the solutions. Based upon a

ranging system that has an intrinsic accuracy of 44 m, we feel that some scaling of the errors of the lunar radii is required and that a 50% increase above the standard error to 15 m, 65 m, and 200 m for the mean, equatorial, and polar radii, respectively, is probably reasonable.

While Table 7 suggests that the mean equatorial radius is well determined, it should be interpreted with caution, as the lunar equator deviates significantly from circularity (cf. Figure 13). The greater scatter in the polar radius solutions arises mostly because of the interpolation over the polar gaps. For this reason, we feel the results from the low-degree solutions (≤ 6) are better because they are less sensitive to the gaps. Note that even with the attendant uncertainty in the solution

Table 5. Comparison of Global Lunar Topography Models

Parameters	Bills and Ferrari [1977]	GLTM 2 (This Study)
Number of observations	5631 Apollo laser 12,342 orbital photo 31 landmark tracking 3311 limb profiles	72,548 Clementine lidar
Total observations	21,999	72,548
Spatial gridding	5°, ~150 km	2°, ~60 km
Spherical harmonic degree	12x12; 1820 km	72x72; 340 km
Regional accuracy	~500 m (nearside only)	~40 m
Accuracy with respect to COM	~1 km	~100 m

that the polar radii are considerably smaller than the equatorial radii and strongly suggest an apparent flattening of about 2 km. We return to this point later.

Low-degree and -order spherical harmonic coefficients. Table 8 summarizes solutions for low-degree and -order spherical harmonic coefficients for a range of topography solutions. The stability of these solutions illustrates clearly that the low-degree and -order shape is well determined from Clementine altimetry.

Center-of-mass/center-of-figure offset. Figure 11 shows solutions for the COM/COF offset. Our analysis shows this offset to be (-1.74, -0.75, 0.27) km in the *x*, *y*, and *z* directions, respectively. It has long been known that the Moon's geometric center was displaced from its center of mass [Kaula *et al.*, 1974; Sjogren and Wollenhaupt, 1976], but as a result of the Clementine altimetry measurements, we know this displacement deviates from the Earth-Moon line. On the farside of the Moon the COM/COF offset is displaced approximately 25° toward the western limb and slightly north of the equator [Zuber *et al.*, 1994], in the general direction of the highlands north of S.P.-Aitken (cf. Plate 1). This displacement, illustrated by a plot of the variation of topography with longitude in Figure 12, is not surprising when viewed in the context of the overall shape of the Moon but is particularly interesting when compared to the lunar gravity field, which shows no such offset from the Earth-Moon line [Lemoine *et al.*, 1996] (F.G. Lemoine *et al.*, A 70th degree and order lunar gravity model from Clementine and historical data, submitted to *Journal of Geophysical Research*, 1996;

hereinafter referred to as submitted paper). Long-wavelength displacements that result from the irregular shape of the Moon are thus isostatically compensated, perhaps largely by variations in crustal thickness [Zuber *et al.*, 1994]. Other density variations within the interior are likely insufficient to accomplish compensation [Neumann *et al.*, 1996; Solomon and Simons, 1996], though probably contribute significantly [Solomon, 1978; Thurber and Solomon, 1978; Wiczorek and Phillips, 1996].

Equatorial ellipticity. Another notable characteristic of the Moon is the lack of any significant ellipticity in the equatorial plane. Figure 13 shows the elevation with respect to a sphere, i.e., deviations from a spheroid for all data within 1° of the equator, along with low-degree and -order spherical harmonic terms evaluated at the equator. The (2,2) terms in the spherical harmonic model indicate an amplitude in the equatorial plane of about 800 m with a maximum ~40°E longitude, smaller than the COM/COF offset, but aligned in

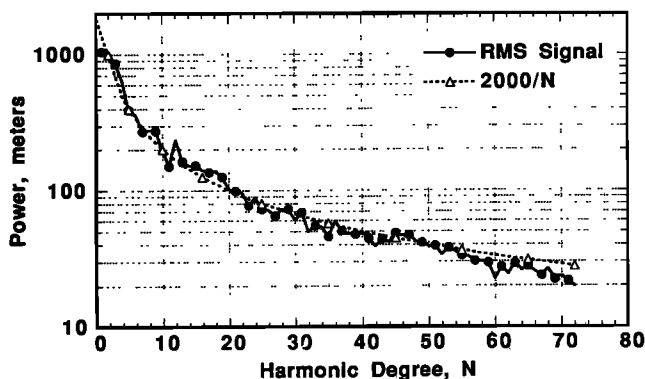


Figure 7. Lunar topographic amplitude spectrum based on Clementine altimetry. Note that the power of topography follows a general relationship of 2 km per spherical harmonic degree *N*.

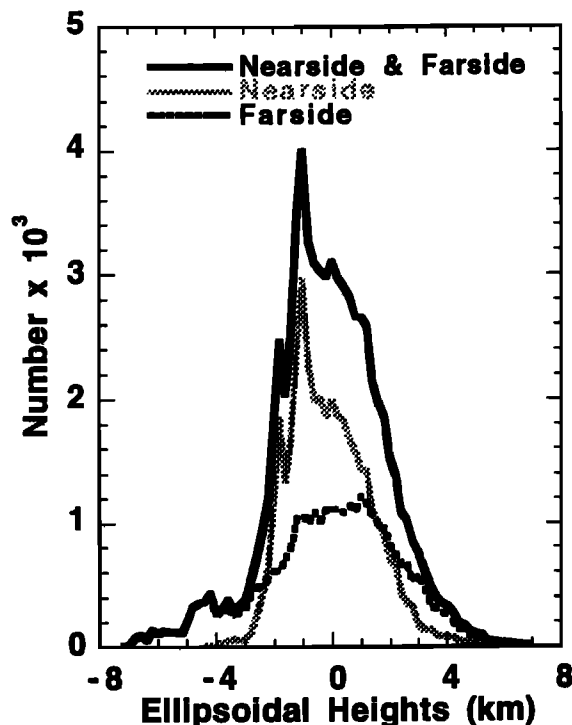


Figure 8. Histograms of ellipsoidal heights of all lunar topography (solid black line), nearside topography (grey solid line), and farside topography (black dotted line).

Table 6. Comparison of Clementine Apollo Laser and Clementine Lidar Profile Data Sets

Parameters	Apollo	Clementine
Number of observations	7080	72,548
Coverage	26S° to 26N°	79S° to 81N°
Along-track resolution	30-43 km	≥20 km
Across-track resolution	NA	~60 km
Single shot vertical resolution	2 m	39.972 m

NA, not available.

the same general direction. Figure 13 also illustrates that the (1,1) terms are more than a factor of 2 larger than the (2,2) terms and indicates that the largest topographic effect around the lunar equator is the COM/COF offset. Further, the major axis of the equatorial ellipticity (2,2 terms) is offset from the Earth-Moon line by about 45° (E) and the (1,1) terms are also offset about 30° (E) and presumably trying to satisfy the fact that the maximum elevation of the highlands is not at longitude 180°E but rather 210°E. While the major axis of the lunar shape does not directly align toward Earth, the minimum moment of the lunar mass does [Ferrari *et al.*, 1980; Dickey *et al.*, 1994].

Triaxial ellipsoid. Because the major axis of lunar topography is not in the Earth-Moon line, we have produced two solutions for the best fit triaxial ellipsoid, which are shown in Table 9. In the first (rotated) solution, we fit the ellipsoid without constraining the direction of any of the axes. This solution best fits all data in a least squares sense and has a major axis that is aligned in the general direction of the highest farside topography and with the polar axis tilted toward Earth and passing through latitude 66.0°N, longitude

10.4°E. In the second (nonrotated) solution, all axes are fixed, with the A axis along 0° longitude, and A and B in the equatorial plane. This solution does not fit the Clementine radii as well as the rotated solution and reduces the size of the longest (A) equatorial axis, probably because the axis will be closer to the S.P.-Aitken basin (cf. Plate 1) while increasing the polar axis (C). Nevertheless, this model suggests a larger equatorial mean radius than polar radius by nearly 2.5 km.

Flattening. The radii measurements have an rms deviation about the best fit (displaced) sphere of 2.1 km with a full dynamic range of nearly 16 km. The radius measurements within ±1° of the equator suggest that the mean equatorial radius is approximately 1.2 ± 0.2 km larger than the mean radius, while the two polar radii are about 0.8 ± 0.5 km less than the mean. This leads to an apparent flattening of 2.0 ± 0.5 km. The large uncertainty arises because the altimetry data do not extend beyond approximately latitudes 81°N and 79°S and extrapolation to the poles is necessary. Further, the local topography in the polar regions is large compared to the flattening and is inseparable from it. Another more definitive

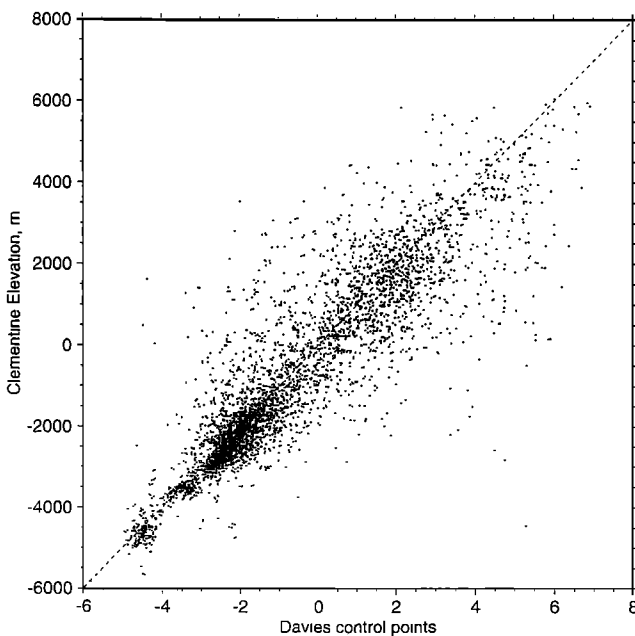


Figure 9. Comparison of elevations from the Clementine and Apollo laser instruments for 5141 points. Deviations from perfect correlation include more accurate orbits determined from Clementine tracking and macroscale roughness of the Moon.

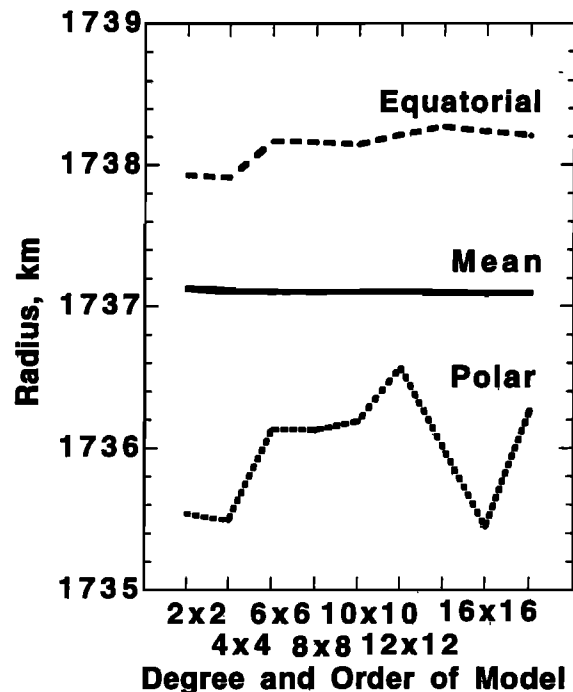


Figure 10. Low-degree and -order spherical harmonic solutions for the Moon's mean, equatorial, and polar radii. The stability of the solutions provides an indication of the confidence of the estimates.

Table 7. Radii and Flattening of the Moon From Low-Degree Spherical Harmonic Models

Spherical Harmonic Model (degree x ordinate)	Mean Radius, km	Equatorial Radius, km	Polar Radius, km	Polar Flattening, km
2x2	1737.129	1737.927	1735.534	2.393
3x3	1737.106	1737.912	1735.494	2.419
4x4	1737.104	1738.171	1736.132	2.040
5x5	1737.100	1738.160	1736.124	2.036
6x6	1737.102	1738.143	1736.187	1.956
8x8	1737.106	1738.216	1736.565	1.651
10x10	1737.096	1738.274	1736.006	2.267
12x12	1737.088	1738.238	1735.445	2.792
16x16	1737.095	1738.208	1736.261	1.947
Mean	1737.103	1738.139	1735.972	2.167
Standard error	0.010	0.044	0.131	0.112

Values are not independent estimates. The standard error only indicates the stability of the solutions.

estimate comes from the even zonal terms of the spherical harmonic solution (Table 7), which yields an apparent flattening of 2.17 ± 0.12 km. This apparent topographic flattening is not to be confused with the hydrostatic flattening of approximately 6 m or the dynamical flattening of about 500 m, which are derived from the rotation and the gravitational potential.

It is essential to note that a major contribution to the Moon's deviation from sphericity comes from the farside equatorial highlands (cf. Plate 1), which are likely a consequence of large-scale melting and/or impact-related redistribution of crustal material [Zuber *et al.*, 1994]. Consequently, there is a significant "geological" contribution to the topographic flattening. We thus refer to the observed flattening as "apparent" because the fundamental shape cannot a priori be ascribed to a "frozen-in" rotational or tidal bulge [Zuber *et al.*, 1996]. In a separate analysis, we have endeavored to identify the magnitude of the geological contribution to the flattening and are in the process of interpreting the residual in the context of the rotational, tidal and thermal history of the Moon (M.T. Zuber and D.E. Smith, manuscript in preparation, 1996).

Major Impact Basins

Large impact basins have imparted significant stochastic variations on the lunar shape. The magnitude of basin

topography is much greater than both the apparent topographic flattening and the equatorial ellipticity, and this imposes a significant challenge in interpreting the fundamental lunar figure. A further complication arises from the fact that the large basins contribute to the flattening and ellipticity, albeit in a random manner. The most pronounced topographic feature on the Moon is the S.P.-Aitken basin, which is characterized by a diameter of 2250 km, a rim-to-floor depth of 8.2 km below the reference ellipsoid, and a 12-km total vertical dynamic range. This structure, which is the largest and deepest known impact basin in the solar system [Spudis *et al.*, 1994; Zuber *et al.*, 1994], was first detected by the Soviet Zond 3 spacecraft measurements [Rodionov *et al.*, 1971] but could not be confirmed (B.G. Bills, personal communication, 1995). The basin was later characterized on the basis of geological mapping of lunar images [Stuart-Alexander, 1978; Wilhelms, 1987]. Figure 14 shows a plot of the ellipsoidal heights (elevation minus best fit ellipsoid) versus latitude. The clear depression in the southern hemisphere that extends from 20°S to 75°S is S.P.-Aitken and illustrates the major influence of this basin on any discussion or computation of the lunar shape. While lunar basins such as Maria Imbrium and Serengetatis also represent spatially extensive depressions and other basins such as Humboldtianum, Crisium, and Fecunditatis constitute significant topographic lows, no other basin is nearly as distinctive on the global scale as S.P.-Aitken.

Table 8. Low-Degree Spherical Harmonic Coefficients (Normalized)

Spherical Harmonic Model (degree x ordinate)	C(2,0), m	C(2,1), m	S(2,1), m	C(2,2), m	S(2,2), m
2x2	-713.53	-812.52	-11.04	68.006	379.27
3x3	-721.13	-822.22	-11.47	67.585	386.05
4x4	-732.00	-773.76	-0.25	81.346	388.12
5x5	-728.77	-775.32	4.26	82.359	385.61
6x6	-731.04	-780.72	0.97	86.642	389.28
8x8	-715.51	-786.93	5.76	81.808	393.10
10x10	-736.75	-784.46	0.85	81.356	396.45
12x12	-755.45	-779.71	2.70	74.620	393.49
16x16	-733.90	-777.24	1.50	72.934	395.92
Mean	-729.79	-780.72	-1.69	77.41	389.70
Standard error	4.21	5.76	2.01	2.28	1.87

Values are not independent estimates. The standard error only indicates the stability of the solutions.

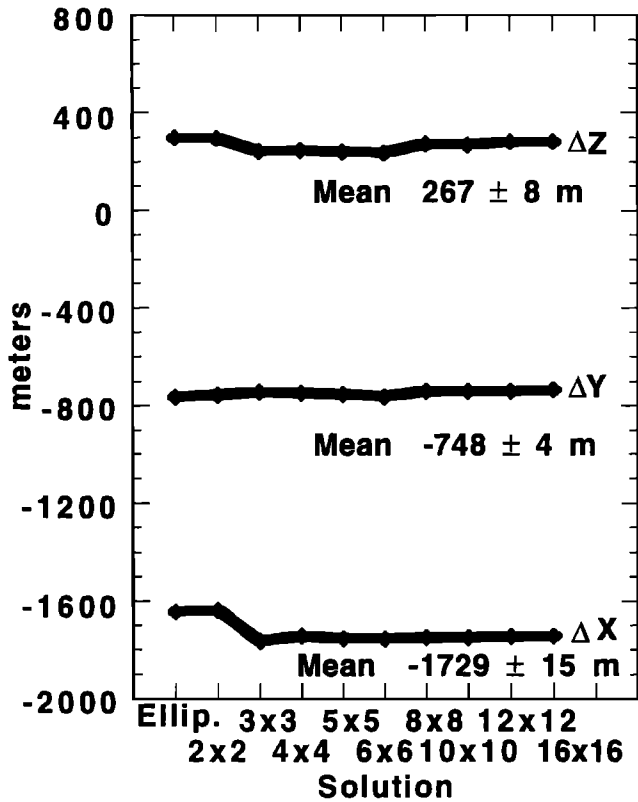


Figure 11. Center-of-mass/center-of-figure offsets in (x,y,z) directions for low-degree and -order spherical harmonic models of lunar topography.

Note that Figure 14 does not show obvious evidence for a previously proposed massive (3200 km diameter) nearside Oceanus Procellarum basin [Wilhelms, 1987]. While support for the existence of this basin has been offered on the basis of Clementine altimetry [McEwen and Shoemaker, 1995],

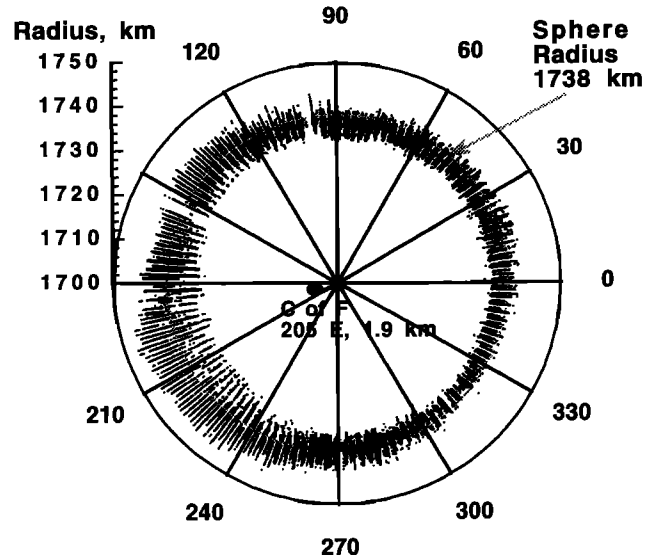


Figure 12. Variation of lunar radii with longitude. The plot shows that the offset between the Moon's center-of-figure and center-of-mass deviates from the Earth-Moon line (0°-180° longitude) and is displaced approximately 25°, such that it is aligned in the direction of the region of highest lunar topography on the farside.

lacking or ambiguous evidence has been cited in other analyses based on altimetry and crustal thickness [Spudis, 1995; Zuber et al., 1995; Neumann et al., 1996]. The lack of a prominent topographic expression in association with the hypothesized structure has been realized since the Apollo era [Kaula et al., 1972, 1973, 1974; Phillips et al., 1973b; Brown et al., 1974]. Indeed, if this basin existed, it must have either undergone virtually complete topographic relaxation and/ or formed prior to at least some nearside highlands which subsequently masked the signature.

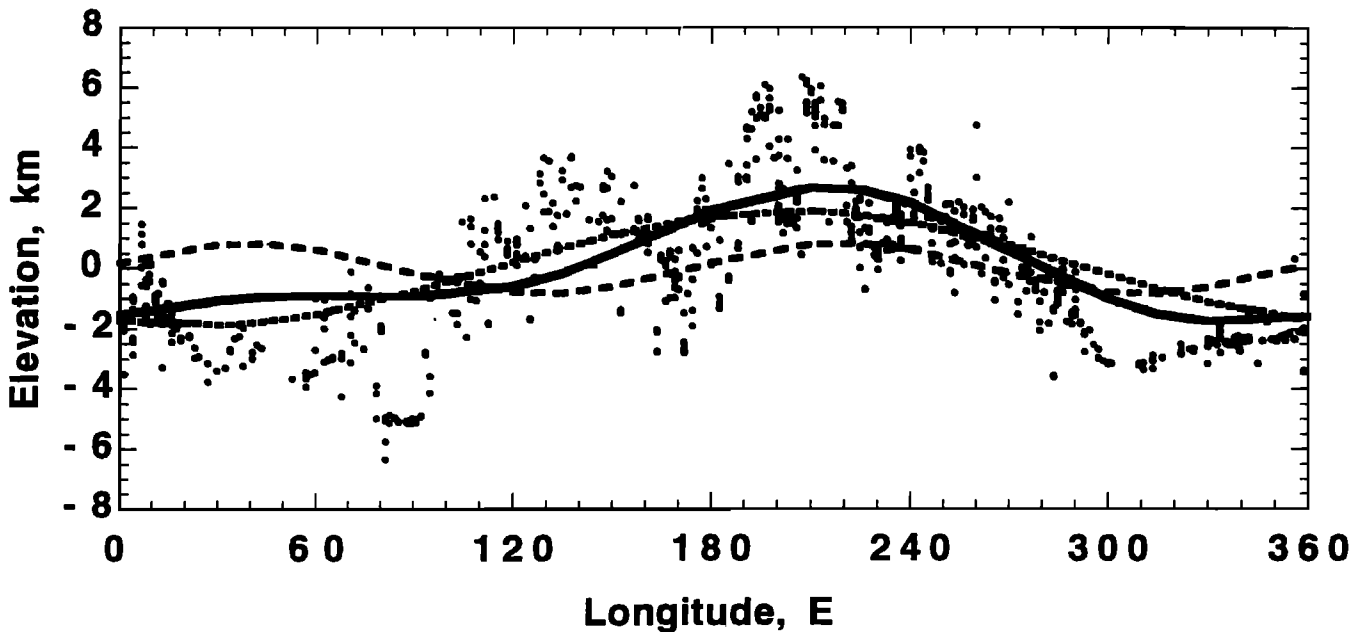


Figure 13. All lunar radii measured by Clementine within 1° of the equator. The values are subtracted from a mean of 1738.0 km. The dotted line shows the (1,1) term of the spherical harmonic expansion of topography and the dashed line shows the (2,2) term. The solid line shows the sum of these terms.

Table 9. Lunar Shape and Topographic Parameters From Analysis of Clementine Altimetry

Parameter	Value, km	Sigma, m
Mean radius*	1737.103	± 15
Mean equatorial radius*	1738.139	± 65
Mean polar radius*	1735.972	± 200
North polar radius†	1736.010	± 300
South polar radius†	1735.840	± 300
Best fit ellipsoid (rotated)		
A axis	1739.020	± 15
B axis	1737.567	± 15
C axis	1734.840	± 65
Best fit ellipsoid (non-rotated)		
A axis	1738.056	± 17
B axis	1737.843	± 17
C axis	1735.485	± 72

* From spherical harmonic solutions (Table 7).

† From spheroidal heights.

One of the puzzling characteristics of the Moon is that nearside basins are filled with mare lavas and farside basins tend to lack volcanic fill [Wilhelms, 1987]. The most obvious possibility is that mare basalt on the Moon may have risen to a hydrostatic level [Runcorn, 1974]. Inherent in this scenario is the assumption of a common magma source depth for all basins, filled and unfilled. If one invokes the usual interpretation that the Moon's COM/COF offset corresponds to a crustal thickness difference, then the nearside crust is thinner than the farside crust. On the nearside the hydrostatic level is located above basin floors, and it would be expected that the elevations of maria would form a gravitational equipotential surface. In contrast, owing to the thicker, low-density crust, the equipotential level on the farside would be deeper in the crust, presumably below basin floors, and magma would not be expected to rise to an elevation that resulted in basin flooding. Preliminary analysis of basin elevations determined from Apollo altimetry [Sjogren and Wollenhaupt, 1976] and radar sounding [Brown *et al.*, 1974] suggested that nearside maria surfaces constituted an equipotential, but the analysis was limited to equatorial basins beneath the Apollo ground tracks. The improved spatial coverage provided by Clementine allows a test of this hypothesis using a globally distributed data set.

Figure 15 plots the elevations of the floors of unflooded basins and mare surfaces of flooded basins as a function of longitude, along with the corresponding geoid elevation (F.G. Lemoine *et al.*, submitted paper) at the center of each basin. Note that maria are parallel to the geoid to within 3 km, equivalent to 500 m on Earth when adjusting for the difference in g . (And all but two mare basins lie within 1 km, equivalent to 160 m on Earth). The fact that the maria surfaces closely parallel the geoid indicates that these surface do indeed define a gravitational equipotential. Also note that with the exception of S.P.-Aitken, unflooded basins tend to be at or above the elevation of the mare surfaces. If a hydrostatic argument is valid, these basins would not be expected to contain mare fill; if they did, it would have been necessary for magma to have risen above the equipotential surface. However, the floor of S.P.-Aitken, which lies from 2 to 6 km below the mare equipotential (and in addition, is underlain by one of the thinnest regions of crust on the Moon [Neumann *et al.*, 1996]), would be expected to contain mare fill, but does not. The Clementine data thus support a hydrostatic mechanism to explain the absence of significant mare fill in farside basins, except for S.P.-Aitken. For this basin it is necessary to invoke alternative arguments such as poor mare production efficiency due to internal compositional or thermal heterogeneity in this part of the early Moon [Lucey *et al.*, 1994].

In Figure 16 we show the relationship between elevation and basin age. Elevations are plotted for the floors of unflooded basins, and the mare surfaces and floor elevations of mare basins, the latter determined by correcting for the thickness of mare fill. We determined fill thicknesses on the basis of a recent analysis of depth-diameter relationships for flooded and unflooded impact basins using Clementine altimetry [Williams and Zuber, 1996]. The figure shows that radial elevations of mare basins tend to correlate, at a statistically significant level, with basin age. This relationship could perhaps be explained if younger basins overlapped on sites of older basins; because such areas had been previously excavated they would have had a lower elevation prior to later impacts. Nonmare basins do not exhibit similar correlation, but their ages are not as well determined as those of the mare basins. In any case, the explanation for this observation will require more detailed modeling and analysis than presented here. We also note that neither mare nor unflooded basin elevations correlate with basin diameter.

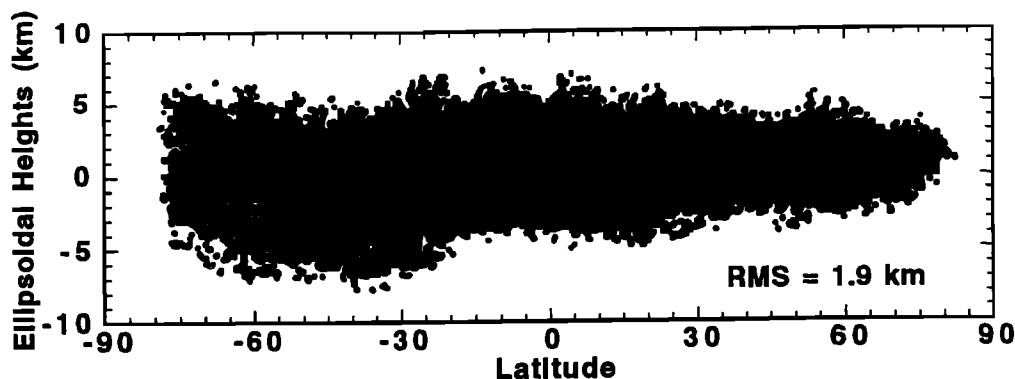


Figure 14. Radially averaged ellipsoidal heights, corresponding to the difference between elevations and the best fit ellipsoid. Note the prominence of the S.P.-Aitken Basin in the southern hemisphere.

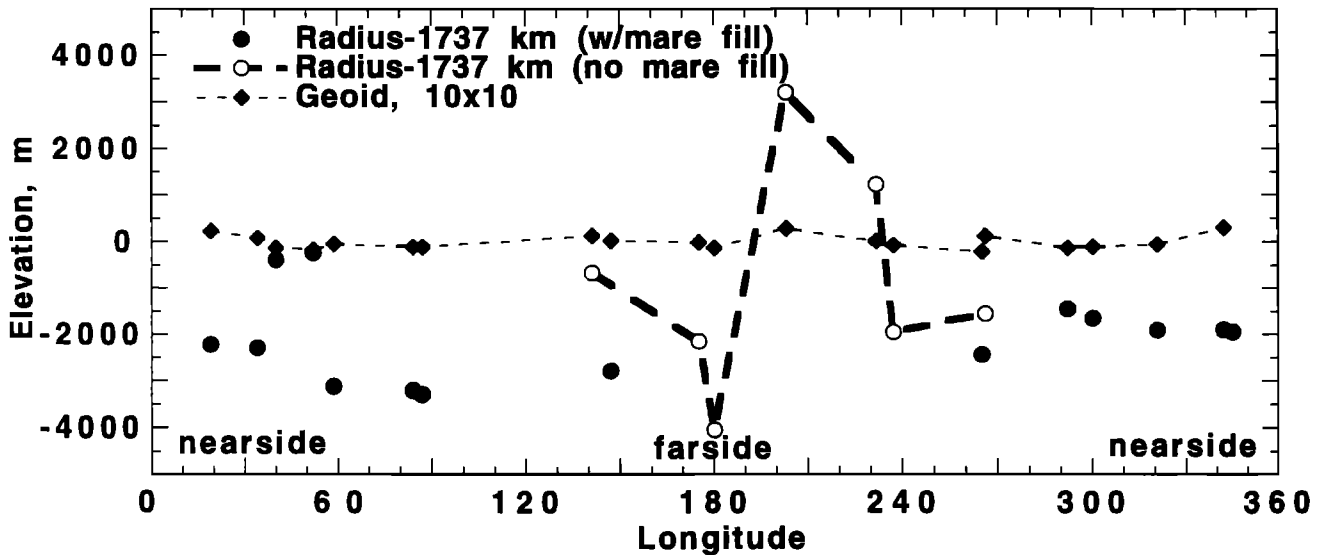


Figure 15. Elevations of the floors of unflooded impact basins (open circles) and mare surfaces of flooded basins (solid circles) as a function of longitude. Also shown is the corresponding geoid elevation at the center of each basin (solid diamonds). Note that with the exception of S.P.-Aitken, the basin floor and mare elevations are parallel to the geoid, indicating that they define an equipotential surface.

Macroscale Surface Roughness

Pre-Clementine analyses of the surface roughness of the Moon [Moore et al., 1976] were driven by assessment of possible manned landing sites, and consequently, focused on much smaller length scales than are resolvable with the Clementine altimetry, which are best suited to analyze wavelengths of tens to hundreds of kilometers. The Kalman filter that we developed to remove noise from the lidar profiles

provided a framework for us to evaluate the Moon's roughness, or local-scale topography, at these wavelengths. We estimated the macroscale surface roughness along the Clementine ground tracks by gridding the lidar-derived topography data into 1/20th degree bins (approximately one shot spacing) along each track, and fitting the local along-track and across-track slopes to the covariance model used in the filtering scheme [Neumann and Forsyth, 1995]. An inherent assumption in this approach is that roughness is

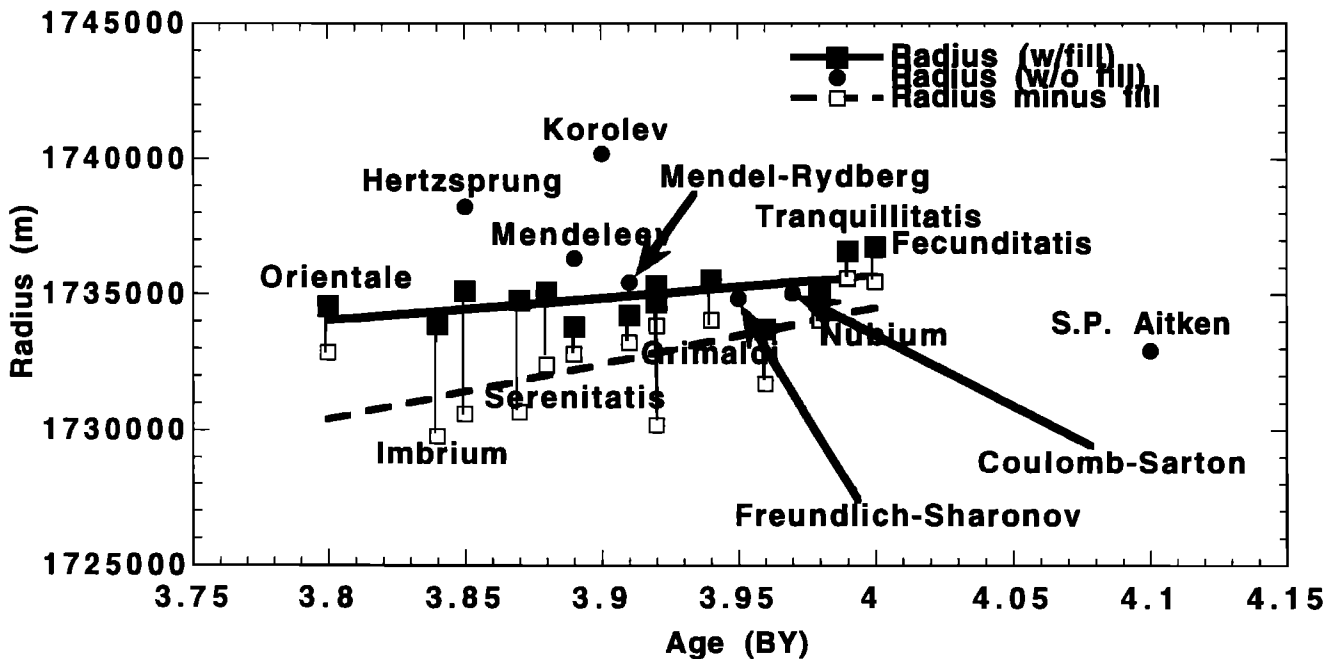


Figure 16. Correlation of basin elevation with age. Results are shown for basins with (solid squares) and without (solid circles) mare fill. Results show a correlation of elevation with age for mare basins. This result persists after correction in which the mare fill is removed (open squares) using the method of Williams and Zuber [1996]. Basins without mare fill do not show any correlation with elevation.

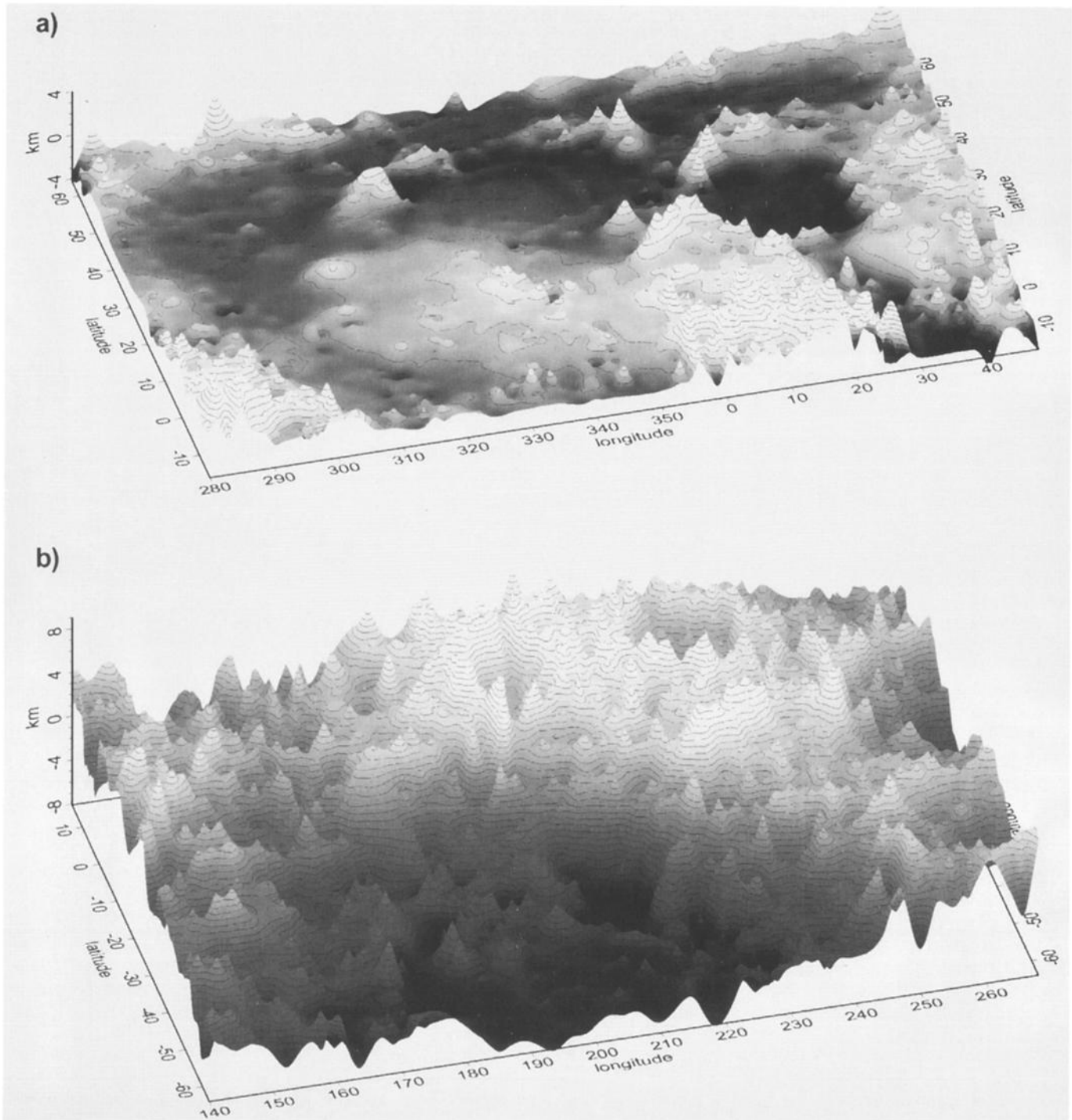


Figure 17. Three-dimensional relief maps of (a) the nearside western hemisphere and (b) the farside S.P.-Aitken basin. The figure illustrates the flatness of lunar maria as compared to the highlands. In Figure 17a the Orientale Cordillera appears at the bottom left with depressions associated with Grimaldi and Cruger along its margin, while Humorum Basin can be seen at the bottom center. The Montes Ural (upper center), Aristarchus Plateau (center), and Montes Carpatius (lower right) rise above the maria. Craters Lichtenberg, Seleucus, Marius, Aristarchus, and Copernicus, from left to right, are resolved as 1- to 2-km-deep depressions. Ptolemaeus appears at the lower right. In Figure 17b the S.P.-Aitken basin covers the central bottom of the figure. For both maps the vertical exaggeration is 60:1.

locally isotropic. The roughness consists of an estimate of the characteristic height, or overall variance, of the sample as a whole, together with an estimate of the distance over which local deviations are expected to attain 80% of this value.

We produced a macroscale roughness map of the Moon in $30^\circ \times 25^\circ$ squares (Figure 6), which shows the marked regional

variability of the best fitting height parameter for topography. A robust measure of incremental variance (h) or median roughness, varies from less than 0.5 km over the northern nearside maria to more than 2 km over the highland regions. The roughness strongly affects the comparability of lidar measurements from different spacecraft ground tracks, and

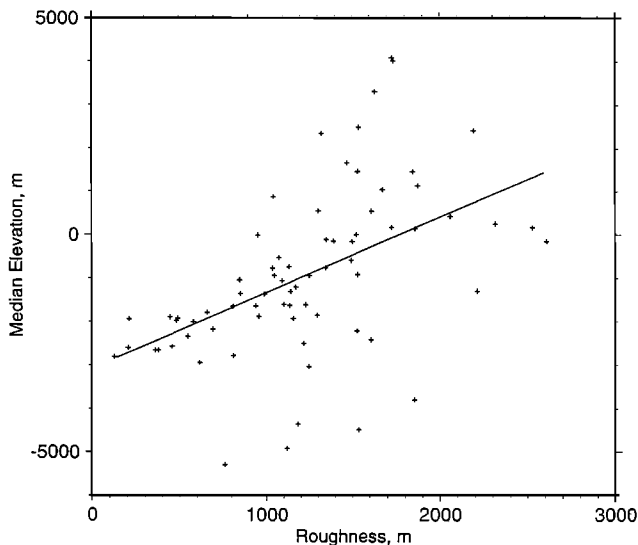


Figure 18. Correlation of lunar surface roughness and elevation. The straight line is a best fit linear regression significant at the 99% level.

accounts for much of the difference between Apollo-era measurements and the Clementine altimetry (Figure 9).

As previously noted from the Apollo altimetry [Kaula *et al.*, 1972], Clementine topography shows the lava-flooded mare basins to be extremely level, with typical slopes less than 1 part in 10^3 . Figure 17a is a 3-D relief map of the nearside western hemisphere, which illustrates the flatness of the northern maria. Over a region of nearly 2400 km², the median absolute deviation of the maria from a smooth (quadratic) surface is only 200 m. Particularly smooth are the northwest Oceanus Procellarum and the Imbrium Basin. Figure 17b illustrates the considerably greater relief of farside highlands in the vicinity of the S.P.-Aitken basin. For comparison, the deviation of this region from a quadratic surface is 2400 m.

As an indicator of the scale of surface processes, the roughness of the Moon appears to reflect more than simply the presence or absence of maria. For example, the S.P.-Aitken basin (180°E, 50°S), an albeit anomalous feature, is topographically smoother than the surrounding highland regions. Factors that correlate with roughness are elevation and age. Figure 18 indicates that the positive correlation between elevation and roughness displays a quasi-linear relationship and is statistically significant at the 99% level. Elevated areas on Earth and Venus also tend to exhibit steeper slopes and greater roughness at generally comparable length scales [Sharpton and Head, 1986; Ford and Pettengill, 1992; Harding *et al.*, 1994; Garvin and Frawley, 1995], though the processes that produced the roughness are distinctive on the various planets.

Summary

Topographic measurements from the Clementine lidar have been used to produce an accurate model for the shape of the Moon. We have analyzed in detail the data and model, with emphasis on spatial resolution, spectral content, and error sources, and have obtained refined estimates of the fundamental parameters of the lunar shape. The largest global-scale features are the center-of-mass/center-of-figure offset and

the apparent polar flattening, both of the order of 2 km. In comparison, the equatorial ellipticity, at 800 m, is small.

Redistribution of crustal material from major impacts has significantly modified the lunar shape, with the magnitude of major impact basin topography exceeding the magnitudes of Moon's long wavelength deviations from sphericity. Mare basin elevations parallel the geoid and thus define a gravitational equipotential surface, while the floors of unflooded large basins, except for S.P.-Aitken, lie above the equipotential. Mare and unflooded basin elevations are consistent with a hydrostatic mechanism for the absence of significant farside maria except for S.P.-Aitken. The observed absence of significant mare deposits in this structure implies major compositional and/or thermal heterogeneity in the lunar interior.

A comparison of elevations derived from the Clementine lidar to control point elevations from the Apollo laser altimeters indicates that measured relative topographic heights generally agree to within ~200 m on the maria. Deviations from a quadratic surface increase to over 2 km on the farside highlands. The observed scatter of the observations is due to noncoincidence of measurements and the roughness of macroscale (10^1 - 10^2 km) topography. Lunar surface roughness at these length scales correlates with surface elevation and age.

The improved knowledge of topography provided by Clementine has implications for lunar structure and evolution. Models of internal structure that require both high-quality topography and gravity measurements will continue to be hampered, at least in the near term, by the lack of farside gravity observations, which require direct Doppler tracking of an orbiting spacecraft. However, both the topography and gravity (F.G. Lemoine *et al.*, submitted paper) data sets are sufficiently improved from pre-Clementine versions to enable many global- and regional-scale problems to be addressed. Of particular value would be the isolation of effects of major impacts, heterogeneous crustal production, and orbital and tidal influence on the long-wavelength shape, in order to understand the contributions of these fundamental processes in the formative development of the Moon.

Acknowledgments. We are grateful to P. Rustan and the Ballistic Missile Defense Organization for implementation of the mission; I. Lewis for providing significant insight concerning the function and operation of the lidar instrument; G. Elman, S. Fricke, E. Pavlis, and A. Brenner for assistance in the data reduction; D. Rowlands for support in the orbit and spacecraft pointing corrections; H.-S. Park for providing the Clementine lidar ground calibration data; H. Taylor for reformatting the raw range data; R. Reisse and C. Acton for information on spacecraft timing errors; J. Garvin for discussions about lunar surface roughness; M. Davies for making available the lunar control network coordinates; and K. Williams for providing basin depths and maria thicknesses. In addition, we thank W. Sjogren for helpful comments and R. Phillips for a detailed review that greatly improved the paper. This work was supported by grants from the NASA/Ballistic Missile Defense Organization Clementine Project, the NASA Planetary Geology and Geophysics Program, and the NASA Lunar and Asteroid Data Analysis Program. Altimetry processing algorithms were developed in support of the Mars Observer and Mars Global Surveyor laser altimetry investigations. The lidar profiles, global grid, and spherical harmonic model are archived in the Geophysics Node of the NASA Planetary Data System at Washington University, St. Louis, Missouri.

References

- Arthur, D. W. G., and P. Bates, The Tucson selenodetic triangulation, *Commun. Luna Planet. Lab.*, 7, 313-361, 1968.
- Baldwin, R. B., *The Face of the Moon*, p. 239, Univ. of Chicago Press, Chicago, Ill., 1949.

- Baldwin, R. B., *The Measure of the Moon*, p. 488, Univ. of Chicago Press, Chicago, Ill., 1963.
- Bell, T. H., Statistical features of sea-floor topography, *Deep Sea Res.*, 22, 883-892, 1975.
- Bills, B. G., and A. J. Ferrari, A harmonic analysis of lunar topography, *Icarus*, 31, 244-259, 1977.
- Bills, B. G., and M. Koblitz, Venus topography: A harmonic analysis, *J. Geophys. Res.*, 90, 827-836, 1985.
- Brown, W. E. J., et al., Elevation profiles of the Moon, *Proc. Lunar Sci. Conf.*, 5th, 3037-3048, 1974.
- Davies, M. E., T. R. Colvin, and D. L. Meyer, A unified lunar control network: The nearside, *J. Geophys. Res.*, 92, 177-184, 1987.
- Davis, J. C., *Statistics and Data Analysis in Geology*, John Wiley, New York, 1973.
- Dickey, J. O., et al., Lunar laser ranging: A continuing legacy of the Apollo program, *Science*, 265, 482-490, 1994.
- Duxbury, T., et al., Pre-launch models of the Clementine spacecraft and remote sensing science instruments for geodesy, cartography and dynamical sciences, *BMDO DSPE Internal Report*, January 1994.
- Ferrari, A. J., W. S. Sinclair, W. L. Sjogren, J. G. Williams, and C. F. Yoder, Geophysical parameters of the Earth-Moon system, *J. Geophys. Res.*, 85, 3939-3951, 1980.
- Ford, P. G., and G. H. Pettengill, Venus topography and kilometer-scale slopes, *J. Geophys. Res.*, 97, 13,103-13,114, 1992.
- Fox, C. G., and D. E. Hayes, Quantitative methods for analyzing the roughness of the seafloor, *Rev. Geophys.*, 23, 1-48, 1985.
- Garvin, J. B., and J. J. Frawley, Topographic ruggedness properties of Venus and Earth, *Geoscientist*, 5, 13-16, 1995.
- Gilbert, L. E., and A. Malinverno, A characterization of the spectral density of residual ocean floor topography, *Geophys. Res. Lett.*, 15, 1401-1404, 1988.
- Goff, J. A., *Stochastic modeling of seafloor topography*, Ph.D. dissertation, Mass. Inst. of Technol., Cambridge, 1990.
- Goff, J. A., and T. H. Jordan, Stochastic modeling of seafloor morphology: Inversion of Sea Beam data for second-order statistics, *J. Geophys. Res.*, 93, 13,589-13,608, 1988.
- Goff, J. A., and T. H. Jordan, Stochastic modeling of seafloor morphology: Resolution of topographic parameters by Sea Beam data, *IEEE J. Oceanic Eng.*, 14, 326-337, 1989a.
- Goff, J. A., and T. H. Jordan, Stochastic modeling of seafloor morphology: A parameterized Gaussian model, *Geophys. Res. Lett.*, 16, 45-48, 1989b.
- Harding, D. J., J. L. Bufton, and J. J. Frawley, Satellite laser altimetry of terrestrial topography: Vertical accuracy as a function of surface slope, roughness, and cloud cover, *IEEE Trans. Geosci. Remote Sens.*, 32, 329-339, 1994.
- Head, J. W., E. Robinson and R. J. Phillips, Topography of the Orientale basin, *Lunar Planet. Sci. Conf.*, XII, 421-423, 1981.
- Hopmann, J., General-Katalog absoluter Hohen auf dem Kond, *Ann. Univ. Sternw. Wien*, 26, 7, 1967.
- Huang, J., and D. L. Turcotte, Fractal mapping of digitized images: Application to the topography of Arizona and comparison to synthetic images, *J. Geophys. Res.*, 94, 7491-7495, 1989.
- Hurst, H. E., Long-term storage capacity of reservoirs, *Trans. Am. Soc. Civ. Eng.*, 116, 770-808, 1951.
- Jones, R. L., Estimates of the Moon's geometry using lunar orbiter imagery and Apollo laser altimeter data, *NASA Tech. Rep.*, TR R-407, 1973.
- Kalman, R. E., A new approach to linear filtering and prediction problems, *Trans. ASME J. Basic Eng. Ser. D*, 83, 35-46, 1960.
- Kaula, W. M., *Theory of Satellite Geodesy*, p. 124, Blaisdell, Waltham, Mass., 1966.
- Kaula, W. M., G. Schubert, R. E. Lingenfelter, W. L. Sjogren, and W. R. Wollenhaupt, Analysis and interpretation of lunar laser altimetry, *Proc. Lunar Sci. Conf.*, 3rd, 2189-2204, 1972.
- Kaula, W. M., G. Schubert, R. E. Lingenfelter, W. L. Sjogren, and W. R. Wollenhaupt, Lunar topography from Apollo 15 and 16 laser altimetry, *Proc. Lunar Sci. Conf.*, 4th, 2811-2819, 1973.
- Kaula, W. M., G. Schubert, R. E. Lingenfelter, W. L. Sjogren, and W. R. Wollenhaupt, Apollo laser altimetry and inferences as to lunar surface structure, *Proc. Lunar Planet. Sci. Conf.*, 5th, 3049-3058, 1974.
- Lemoine, F. G., D. E. Smith, M. T. Zuber, D. D. Rowlands, and G. A. Neumann, Results from the Clementine lunar geodesy investigation, *Astrodynamics*, 90, 201-223, 1995.
- Lemoine, F. G., D. E. Smith, M. T. Zuber, and G. A. Neumann, High degree and order spherical harmonic gravity modeling of the Moon from Clementine and historical S-band data, in *Global Gravity Field and Its Temporal Variations*, edited by R. Rapp, A. Cazenave, and R. Nerem, Springer-Verlag, New York, 1996.
- Lucey, P. G., P. D. Spudis, M. Zuber, D. Smith, and E. Malaret, Topographic-compositional units on the Moon and the early evolution of the lunar crust, *Science*, 266, 1855-1858, 1994.
- Malinverno, A., Inverse square-root dependence of mid-ocean-ridge flank roughness on spreading rate, *Nature*, 352, 58-60, 1991.
- Mandelbrot, B., Stochastic models for the Earth's relief, the shape and the fractal dimensions of the coastlines, and the number-area rule for islands, *Proc. Natl. Acad. Sci.*, 72, 3825-3828, 1975.
- Mandelbrot, B., *The Fractal Geometry of Nature*, p. 468, W. H. Freeman, New York, 1982.
- Matherton, G., *Les Variables Regionalisees et Leur Estimation, Une Application de la Theorie des Fonctions Aleatoires aux Sciences de la Nature*, p. 306, Masson, Paris, 1965.
- McCarthy, J. J., S. Rowton, D. Moore, S. Luthcke, D. E. Pavlis, L. S. Tsaoussi, D. D. Rowlands, and J. A. Marshall, GEODYN systems descriptions and operations manuals, Contractor Rep., NASA Goddard Space Flight Cent. and Hughes/STX, Greenbelt, Md., 1994.
- McEwen, A. S., and E. M. Shoemaker, Two classes of impact basins on the Moon (abstract), *Lunar Planet. Sci. Conf.*, XXVI, 935-936, 1995.
- Mills, G. A., and P. V. Sudbury, Absolute coordinates of lunar features, *Icarus*, 9, 538-561, 1968.
- Moore, H. J., G. L. Tyler, J. M. Boyce, R. W. Shorthill, T. W. Thompson, D. E. Wilhelms, and S. S. C. Wu, Correlation of photogeology and remote sensing data along Apollo 14, 15 and 16 bistatic radar ground tracks, *U.S. Geol. Survey Open File Report*, 76-298, 101 pp., April 1976.
- Neumann, G. A., and D. W. Forsyth, High resolution statistical estimation of seafloor morphology: Oblique and orthogonal fabric on the mid-Atlantic ridge, *Mar. Geophys. Res.*, 17, 221-250, 1995.
- Neumann, G. A., M. T. Zuber, D. E. Smith, and F. G. Lemoine, The lunar crust: Global signature and structure of major basins, *J. Geophys. Res.*, 101, 16,841-16,863, 1996.
- Nozette, S., et al., The Clementine mission to the Moon: Scientific overview, *Science*, 266, 1835-1839, 1994.
- Phillips, R. J., et al., Apollo lunar sounder experiment, in *Apollo 17 Preliminary Science Report*, pp. 1-26, NASA, Greenbelt, Md., 1973a.
- Phillips, R. J., et al., The Apollo 17 Lunar Sounder, *Proc. Lunar Planet. Sci. Conf.*, 4th, 2821-2831, 1973b.
- Press, W. J., B. P. Flannery, S. A. Teukolsky, and W. T. Vetterling, *Numerical Recipes*, p. 818, Cambridge Univ. Press, New York, 1986.
- Putney, B. H., General Theory for Dynamic Satellite Geodesy, in *The National Geodetic Satellite Program, NASA Spec. Publ.*, SP-365, 1977.
- Regeon, P. A., R. J. Chapman and R. Baugh, Clementine: The Deep Space Program science experiment, *Rep. IAA-L-0501*, pp. 1-13, Int. Acad. of Astron., 1994.
- Roberson, F. I., and W. M. Kaula, Apollo 15 laser altimeter, *Apollo 15 Preliminary Science Report, NASA Spec. Publ.*, SP-289, 25, 48-50, 1972.
- Rodionov, B. N., et al., New data on the Moon's figure and relief based on results from the reduction of Zond-6 photographs, *Cosmic Res.*, 9, 410-417, 1971.
- Runcorn, S. K., On the origin of mascons and moonquakes, *Proc. Lunar Planet. Sci. Conf.*, 5th, 3115-3126, 1974.
- Runcorn, S. K., and B. M. Gray, The figure of the Moon, in *Mantles of the Terrestrial Planets*, pp. 165-173, John Wiley, New York, 1967.
- Runcorn, S. K., and S. Hofmann, The shape of the Moon, in *The Moon*, edited by S. K. Runcorn and H. C. Urey, pp. 22-31, D. Reidel, Norwell, Mass., 1972.
- Runcorn, S. K., and M. H. Shubsall, The figure of the Moon, *Phys. Earth Planet. Inter.*, 1, 317-325, 1968.
- Runcorn, S. K., and M. H. Shubsall, The figure of the Moon, *Phys. Earth Planet. Inter.*, 1, 317-325, 1970.
- Sayles, R. S., and T. R. Thomas, Surface topography as a nonstationary random process, *Nature*, 271, 431-434, 1978.
- Sharpton, V. L., and J. W. Head, A comparison of the regional slope characteristics of Venus and Earth: Implications for geologic processes on Venus, *J. Geophys. Res.*, 91, 7545-7554, 1986.
- Sjogren, W. L., and W. R. Wollenhaupt, Lunar shape via the Apollo laser altimeter, *Science*, 179, 275-278, 1973.
- Sjogren, W. L., and W. R. Wollenhaupt, Lunar global figure from mare surface elevations, *Moon*, 15, 143-154, 1976.

- Smith, W. H. F., and P. Wessel, Gridding with continuous curvature splines in tension, *Geophysics*, 55, 293-305, 1990.
- Solomon, S. C., The nature of isostasy on the Moon: How big a Pratt-fall for Airy models?, *Proc. Lunar Planet. Sci. Conf.*, 9th, 3499-3511, 1978.
- Solomon, S. C., and M. Simons, The isostatic state of the lunar highlands from spatio-spectral localization of gravity, topography and surface chemistry (abstract), *Lunar Planet. Sci. Conf.*, XXVII, 1245-1246, 1996.
- Spudis, P. D., Clementine laser altimetry and multi-ring basins on the Moon (abstract), *Lunar Planet. Sci. Conf.*, XXVI, 1337-1338, 1995.
- Spudis, P. D., R. A. Riese, and J. G. Gillis, Ancient multiring basins on the Moon revealed by Clementine laser altimetry, *Science*, 266, 1848-1851, 1994.
- Stuart-Alexander, D. E., Geologic map of the central farside of the Moon, *U.S. Geol. Surv. Map*, I-1047, 1978.
- Tarantola, A. and B. Valette, Generalized nonlinear inverse problems solved using the least squares criterion, *Rev. Geophys.*, 20, 219-232, 1982.
- Thurber, C. H., and S. C. Solomon, An assessment of crustal thickness variations on the lunar near side: Models, uncertainties, and implications for crustal differentiation, *Proc. Lunar Planet. Sci. Conf.*, 9th, 3481-3497, 1978.
- Watts, C. B., The marginal zone of the Moon, *Astron. Pap. Amr. Ephemeris Naut. Almanac*, 17, 1963.
- Wieczorek, M. A., and R. J. Phillips, The structure and compensation of the lunar highland crust (abstract), *Lunar Planet. Sci. Conf.*, XXVII, 1431-1432, 1996.
- Wilhelms, D. E., *The Geologic History of the Moon*, 302 pp., U.S. Govt. Print. Off., Washington, D.C., 1987.
- Williams, K. K., and M. T. Zuber, Re-evaluation of mare thicknesses based on lunar crater depth-diameter relationships (abstract), *Lunar Planet. Sci. Conf.*, XXVII, 1441-1442, 1996.
- Wollenhaupt, W. R., and W. L. Sjogren, Apollo 16 Laser Altimeter, in *Apollo 16 Preliminary Science Report*, NASA Spec. Publ., SP-315, 30: 1-5, 1972.
- Wollenhaupt, W. R., R. K. Osburn, and G. A. Ransford, Comments on the figure of the Moon from landmark tracking, *Moon*, 5, 149-157, 1972.
- Wollenhaupt, W. R., W. L. Sjogren, R. E. Lingenfelter, G. Schubert, and W. M. Kaula, Apollo 17 laser altimeter, in *Apollo 17 Preliminary Science Report*, NASA Spec. Publ., SP-315, 33, 41-43, 1974.
- Zisk, S. H., A new, Earth-based radar technique for the measurement of lunar topography, in *Conference on Lunar Geophysics*, pp. 296-306, Lunar Planet. Inst., Houston, Tex., 1971.
- Zisk, S. H., A new, Earth-based radar technique for the measurement of lunar topography, *Moon*, 4, 296-306, 1972.
- Zuber, M. T., D. E. Smith, F. G. Lemoine, and G. A. Neumann, The shape and internal structure of the Moon from the Clementine mission, *Science*, 266, 1839-1843, 1994.
- Zuber, M. T., D. E. Smith, G. A. Neumann, and F. G. Lemoine, Gravity, topography and the geophysics of the Moon from the Clementine mission (abstract), *Lunar Planet. Sci. Conf.*, XXVI, 1581-1582, 1995.
- Zuber, M. T., D. E. Smith, G. A. Neumann, and F. G. Lemoine, What factors control the long wavelength shape of the Moon? (abstract), *Lunar Planet. Sci. Conf.*, XXVII, 1511-1512, 1996.

F.G. Lemoine, Space Geodesy Branch, Code 926, NASA/Goddard Space Flight Center, Greenbelt, MD 20771. (lemoine@olympus.gsfc.nasa.gov)

G.A. Neumann, Department of Earth and Planetary Sciences, Johns Hopkins University, Baltimore, MD 21218. (neumann@utopia.eps.jhu.edu)

D.E. Smith, Laboratory for Terrestrial Physics, Code 920, NASA/Goddard Space Flight Center, Greenbelt, MD 20771. (dsmith@tharsis.gsfc.nasa.gov)

M.T. Zuber, Department of Earth, Atmospheric and Planetary Sciences, Massachusetts Institute of Technology, Cambridge, MA 02139-4307. (zuber@mit.edu)

(Received June 24, 1996; revised September 16, 1996; accepted September 18, 1996.)